



Diagnosing the Scale and Space Dependent Horizontal Eddy

Diffusivity at the Global Surface Ocean

Aleksi Nummelin*[†]

*Department of Earth and Planetary Sciences, Johns Hopkins University, Baltimore,
Maryland*

Julius J. M. Busecke

*Department of Earth and Environmental Sciences, Columbia University, New York, New
York, and Department of Geosciences, Princeton University, Princeton, New Jersey*

Thomas W. N. Haine

*Department of Earth and Planetary Sciences, Johns Hopkins University, Baltimore,
Maryland*

Ryan P. Abernathey

*Department of Earth and Environmental Sciences, Columbia University, New York, New
York*

**Corresponding author:* Aleksi Nummelin, aleksi.h.nummelin@gmail.com

[†]Current affiliation: NORCE the Norwegian Research Centre AS, Bergen, Norway

Early Online Release: This preliminary version has been accepted for publication in *Journal of the Physical Oceanography*, may be fully cited, and has been assigned DOI 10.1175/JPO-D-19-0256.1. The final typeset copyedited article will replace the EOR at the above DOI when it is published.

ABSTRACT

Oceanic tracers are transported by oceanic motions of all scales, but only the large scale motions are resolved by the present-day Earth System Models. In these models, the unresolved lateral sub-gridscale tracer transport is generally parameterized through diffusive closures with a scale-independent diffusion coefficient. However, evidence from observations and theory suggests that diffusivity varies spatially and is length-scale dependent. Here we provide new scale-dependent quantification of the global surface diffusivities. To this end we use a recently developed statistical inversion method, MicroInverse, to diagnose horizontal surface diffusivities from observed sea surface temperature and idealized model simulation. We compare the results to theoretical estimates of mixing by the large scale shear and by the sub-gridscale velocity fluctuations. The diagnosed diffusivity magnitude peaks in the tropics and western boundary currents with minima in the sub-tropical gyres ($\sim 3000 \text{ m}^2\text{s}^{-1}$ and $\sim 100 \text{ m}^2\text{s}^{-1}$) at $\sim 40 \text{ km}$ scale, respectively. Focusing on the 40-200 km length scale range, we find that the diffusivity magnitude scales with the length scale to a power (n) that is between 1.22-1.54 (90% confidence) in the tropics and also peaks at values above 1 in the boundary currents. In the midlatitudes we find that $0.58 < n < 0.87$ (90% confidence). Comparison to the theory suggests that in regions with $n > 1$ the horizontal mixing is dominated by large scale shear, whereas in regions where $n < 1$ the horizontal mixing is due to processes that are small compared to the 40-200 km length scale range considered in this study.

1. Introduction

Ocean modelers discretize the equations of fluid dynamics on a grid, which requires parameterizing the processes at scales smaller than the resolved grid size (Fox-Kemper et al. 2019). These processes include vertical and horizontal transport of momentum and tracers by sub-gridscale processes. Our focus here is on the horizontal tracer transport, which is commonly parameterized using a flux-gradient relationship, i.e., the tracer flux is taken to be proportional to the product of the large scale tracer gradient and a diffusion tensor. Whereas the large scale tracer gradient is straightforward to diagnose, the diffusion tensor is poorly constrained by observations despite its importance for biogeochemistry and climate (Gnanadesikan et al. 2015, 2017). Various estimates for ocean tracer diffusivity exist, but an empirical and length scale dependent estimate is lacking. To this end we provide a global, spatially-varying, empirical estimate of the magnitude of the diffusion tensor and its dependence on the spatial scale at the ocean surface. We base our estimates on satellite observations, a tracer simulation, and a recently developed statistical inversion methodology (MicroInverse, Nummelin et al. 2018; see also Jeffress and Haine 2014a,b). While this paper and its supplement introduces the MicroInverse method, we encourage the readers who are interested in understanding the method in detail to read Nummelin et al. (2018).

In its general form the flux-gradient tracer flux $\mathbf{F}_{\mathbf{K}}$ is

$$\mathbf{F}_{\mathbf{K}} = -\nabla \cdot (\mathbf{K}_t \nabla \chi) \quad (1)$$

where \mathbf{K}_t is the diffusion tensor and χ is the scalar tracer field in question. The full tensor \mathbf{K}_t is often divided into an antisymmetric (advective) part \mathbf{K}_a and a symmetric (diffusive) part \mathbf{K} . We focus on the magnitude ($\kappa = \|\mathbf{K}\| = \sqrt{\kappa^x \kappa^y}$, where κ^x and κ^y are the east-west

and north-south components of the tensor) of the symmetric horizontal tensor \mathbf{K} at the ocean surface (see Appendix A for effects of the mean flow on the tensor components).

Observational and model-based evidence suggest that κ varies in space both at the ocean surface (Shuckburgh et al. 2009; Marshall et al. 2006; Abernathey and Marshall 2013; Zhurbas et al. 2014; Klocker and Abernathey 2014; Busecke et al. 2017; Nummelin et al. 2018), and at depth (Smith and Marshall 2009; Abernathey et al. 2010; Vollmer and Eden 2013; Cole et al. 2015; Roach et al. 2018; Bachman et al. 2020). Surface diffusivity also varies in time with the atmospheric forcing (Shuckburgh et al. 2009; Busecke and Abernathey 2019). Despite the various methods for estimating lateral diffusivity (see section 2), the magnitude of the diffusion ranges between $\mathcal{O}(100) - \mathcal{O}(10000)$ $\text{m}^2 \text{s}^{-1}$ and is surface intensified (op. cit.). However, the above estimates are dominated by the most energetic scales of the flow (Shuckburgh et al. 2009), whereas we will provide a new scale-aware observational estimate of lateral surface diffusivity.

Observations and theory also provide evidence for the length scale dependence of κ . Mixing length theory (Prandtl 1925; Vallis 2006), suggests that κ should scale with velocity fluctuation ($u_{rms} = \sqrt{u'^2 + v'^2}$; where u' and v' are the high-pass filtered east-west and north-south velocity components, respectively) and a characteristic length scale (l_{eddy}) as

$$\kappa \sim u_{rms} l_{eddy}. \quad (2)$$

Because larger eddies tend to be more energetic than smaller eddies, the mixing length theory suggests that $\kappa \sim l_{eddy}^n$ where $n > 1$. Specifically, at scales smaller than the deformation radius, i.e. within the *enstrophy inertial subrange*, kinetic energy grows rapidly with length scale and one finds $\kappa \sim l^2$ (where l is a inverse wavenumber Vallis 2006). At scales larger than the deformation radius, i.e. within the *energy inertial subrange*, kinetic energy increase

with length scale is more modest and one finds $\kappa \sim l^{4/3}$ (Weizsäcker 1948; Vallis 2006). We will discuss these theoretical relations in more detail in section 2.b.

Observations suggest that both the energy inertial subrange and the enstrophy inertial subrange describe the kinetic energy spectra in parts of the world oceans. For example, Okubo (1971) synthesized observations of tracer (mostly rhodamine dye) spreading between 1 m - 1000 km scales at the surface ocean. He found a power-law scaling between diffusivity and length scale, with an exponent of 1.15 similar to, albeit smaller than, $4/3$ suggested by the energy inertial subrange. Similar exponents are found in more recent studies, both with observations (Ollitrault et al. 2005; van Sebille et al. 2015) and models (Bracco et al. 2018). Ollitrault et al. (2005) find support for a l^2 scaling in Lagrangian float observations at scales below 40 km at 700 dbar depth in the eastern North Atlantic, but generally, there is much less observational evidence for such an enstrophy inertial subrange scaling. Moreover, despite the theoretical, observational, and model based work, there are no estimates (to our knowledge) of the spatial variability of the diffusivity-length scale relationship in the global ocean which we provide here.

As we move towards global coupled climate models at resolutions that are eddy-permitting/resolving at low latitudes, but eddy suppressing at high latitudes, the diffusivity-length scale relationship becomes important and should guide the development of scale-aware eddy-diffusivity and momentum closures (Hallberg 2013; Zanna et al. 2017; Bachman et al. 2017b; Pearson et al. 2017; Jansen et al. 2019; Bachman 2019; Zanna 2019). For example, several global earth system models participating in the Coupled Model Intercomparison Project (CMIP) simulations use spatially uniform diffusion coefficients in their ocean models (see <https://es-doc.org> for CMIP6 and Farneti et al. 2015 for CMIP5 models). Furthermore, most models that use the Gent-McWilliams (Gent and McWilliams 1990; Gent et al.

1995) and Redi (Redi 1982) mesoscale eddy parameterization assume that the eddy induced transport and diffusion coefficients (κ_{GM} and κ_{REDI} , respectively) are the same although it remains unclear how the two are related. Similarly, the recent suggestions for scale-aware parameterizations cited above do not consider scale dependence of tracer diffusivity.

Here we provide a global, empirical, scale-dependent, estimate of κ at the ocean surface. It is based on satellite observations of sea surface temperature and idealized tracer simulations. We also compare our diffusivity estimate to theory in order to assess which processes contribute to mixing in different ocean regions.

The paper is structured as follows: in section 2.a we present the MicroInverse method we use to estimate κ (see also the supplementary material and Nummelin et al. 2018) and in 2.b we review theory that links diffusivity to the kinetic energy spectra. Appendix A provides a link between the magnitude of the diffusivity tensor (focus of this paper) and suppressed across stream diffusivity (discussed in the literature). In sections 3 we shortly present the data sources, but give more details in Appendix B. We present the main results for diagnosed diffusivity fields and their length scale dependence in section 4.a-b and compare our results to theoretical estimates of sub-gridscale diffusivity in section 4.c (see Appendix C for background to the theoretical diffusivity estimates). We summarize and discuss our results in a wider context of sub-gridscale parameterizations in section 5.

2. Theory and Methods

The magnitude of the diffusion tensor, κ , can be estimated with tracer methods such as the effective diffusivity (Nakamura 1996; Shuckburgh et al. 2009, and references therein) and the Osborn-Cox diffusivity (Osborn and Cox 1972; Abernathey and Marshall 2013), with Lagrangian drifter statistics (see LaCasce 2008, for a review, and Klocker et al. 2012b;

Wagner et al. 2019 for comparison of drifter and tracer based methods), or with the mixing-length framework (e.g. Armi and Stommel 1983; Cole et al. 2015). Yet another approach is to use linear stability analysis (Vollmer and Eden 2013). All these estimates describe the intensity of mixing in the flow, but they are not well suited for estimating sub-gridscale diffusivity at a given scale, because they are dominated by the most energetic scales of the flow (Shuckburgh et al. 2009). A more comprehensive approach is to estimate the full diffusion tensor \mathbf{K}_t using multiple tracers (Abernathy et al. 2013; Bachman and Fox-Kemper 2013; Bachman et al. 2015, 2017a, 2020). This multiple tracer approach has been applied successfully in models, but it is difficult to apply to observations because it requires multiple tracers with different orientations to the mean flow. We use the *MicroInverse* method (Nummelin et al. 2018), which is scale dependent and requires only one tracer field.

We collect the different symbols and terminology in table 1 which the reader might find helpful when reading this section.

a. MicroInverse

MicroInverse uses the spatial covariances in a tracer field to estimate \mathbf{K} . Our estimates are based on the satellite records of sea surface temperature and idealized tracer simulations (see section 2.5 for a description of the data). Here we provide a summary of the *MicroInverse* methodology and further details can be found in Nummelin et al. (2018) and in the supplementary material.

Assuming that the time (t) evolution of anomalies in a tracer field (\mathbf{x}) behaves as a linear system with a stochastic forcing (\mathbf{f}) we can write:

$$\frac{d}{dt}\mathbf{x}(t) = \mathbf{B}\mathbf{x}(t) + \mathbf{f}(t), \quad (3)$$

where $\mathbf{x}(t)$ is a $M \times 1$ vector of tracer anomalies at M spatial locations, \mathbf{B} is a constant $M \times M$ matrix operator containing all the processes acting on the tracer field, and $\mathbf{f}(t)$ is the $M \times 1$ stochastic forcing vector, representing the sources and sinks of tracer anomalies.

The goal is to solve for \mathbf{B} (Herterich and Hasselmann 1987; Penland and Magorian 1993; Penland and Sardeshmukh 1995; Piterbarg and Ostrovskii 1997; Penland and Matrosova 1998; Ostrovskii and Piterbarg 2000; Ostrovskii and Font 2003; Deser et al. 2003; Newman 2007; Alexander et al. 2008; Zanna 2012; Penland and Hartten 2014). We assume that the forcing \mathbf{f} has a shorter auto-correlation timescale than the tracer \mathbf{x} , which allows us to write (see Nummelin et al. 2018, for derivations)

$$\mathbf{B} = \frac{1}{\tau} \log \left([\mathbf{x}(t + \tau)\mathbf{x}^T(t)] [\mathbf{x}(t)\mathbf{x}^T(t)]^{-1} \right). \quad (4)$$

Here, the multiplication of \mathbf{x} by its transpose (\mathbf{x}^T) results in covariance matrices, τ is a lead time, $[\cdot]^{-1}$ denotes a matrix inverse, and \log denotes a matrix natural logarithm. We assume that the lead time τ is in-between the auto-correlation timescales of the forcing (\mathbf{f}) and the response (\mathbf{x}).

Whereas (4) is based on a continuous infinite tracer timeseries $\mathbf{x}(t)$, in reality we only possess finite, noisy timeseries. We can therefore only derive an estimate of the response function. Moreover, naive computation of (4) is problematic because (i) the matrix inverse scales poorly with M and (ii) the resulting \mathbf{B} estimate is unreasonably sensitive to spurious far-field covariances. In other words, (4) does not exploit the assumption that \mathbf{B} represents a *local* differential operator. Therefore, we estimate \mathbf{B} iteratively for each of the M points of interest using a modified version of (4) that replaces the $M \times M$ matrices in the argument to the matrix logarithm with (small) $P \times P$ matrices local to each point of interest. Here, we use a 5-point stencil ($P = 5$; 4 cells surrounding the central $[i, j]$ cell at right angles,

see Fig. 1) and denote the locally-estimated properties with a hat, $\hat{\mathbf{B}}$. See Herterich and Hasselmann (1987); Ostrovskii and Piterbarg (2000); Ostrovskii and Font (2003); Jeffress and Haine (2014b) and Nummelin et al. (2018) for similar approaches and discussion. In many predictability applications the problem is simplified by using a reduced basis set e.g., empirical orthogonal functions (Penland and Magorian 1993, and references therein) or by using large scale averages (Frankignoul et al. 1998). Such approaches can be successful for prediction, but they cannot be used for local parameter inversion, which is the goal here.

The final step is to connect $\hat{\mathbf{B}}$ to ocean kinematics. We assume that the time evolution of the tracer field is governed by an advection-diffusion-relaxation operator (see the supplementary material of this paper and Nummelin et al. 2018, for details):

$$\hat{\mathbf{B}} \iff \hat{\mathbf{U}} \cdot \nabla - \nabla \cdot \hat{\mathbf{K}} \nabla - \hat{\mathbf{r}}. \quad (5)$$

Here $\hat{\mathbf{U}}$ is the time mean velocity vector, $\hat{\mathbf{K}}$ is the time mean diffusion tensor, and $\hat{\mathbf{r}}$ is the time mean decay rate. We solve for the diffusion tensor, the velocity vector (that describes the velocity at which the anomalies propagate; including contributions from both resolved and sub-gridscale velocities), and the decay timescale by discretizing (5) on the local $P \times P$ (Fig. 1) stencil using central differences. This leads to the following system of equations

$$\begin{aligned} \hat{B}_{i,j+1}^{l+2} &= \frac{\hat{\kappa}^y}{\Delta y^2} - \frac{1}{2\Delta y} \left(\hat{v} - \frac{\Delta \hat{\kappa}^y}{\Delta y} \right) \\ \hat{B}_{i+1,j}^{l+1} &= \frac{\hat{\kappa}^x}{\Delta x^2} - \frac{1}{2\Delta x} \left(\hat{u} - \frac{\Delta \hat{\kappa}^x}{\Delta x} \right) \\ \hat{B}_{i,j}^l &= -\frac{2\hat{\kappa}^x}{\Delta x^2} - \frac{2\hat{\kappa}^y}{\Delta y^2} - \hat{r} \\ \hat{B}_{i-1,j}^{l-1} &= \frac{\hat{\kappa}^x}{\Delta x^2} + \frac{1}{2\Delta x} \left(\hat{u} - \frac{\Delta \hat{\kappa}^x}{\Delta x} \right) \\ \hat{B}_{i,j-1}^{l-2} &= \frac{\hat{\kappa}^y}{\Delta y^2} + \frac{1}{2\Delta y} \left(\hat{v} - \frac{\Delta \hat{\kappa}^y}{\Delta y} \right), \end{aligned} \quad (6)$$

where Δx and Δy are the horizontal grid sizes of the data in the x and y directions. The $\hat{\mathbf{B}}$ in (5) is a local $P \times P$ matrix defined by (4) and its relevant elements are those that depend on cross-covariances between the central point (i, j) and the surrounding points on the local stencil (Fig. 1). These elements are collected in vector \hat{B} in (6). The \hat{B} superscripts refer to the vector indices whereas the subscripts refer to the corresponding index in the stencil (Fig. 1). From (6) we solve for the 5 unknowns (2 components of velocity and diffusivity, and the decay timescale). For brevity, we focus on the Cartesian components of $\hat{\mathbf{K}}$ that are relevant here:

$$\begin{aligned}\hat{\kappa}^x &= \frac{\Delta x^2}{2} \left(\hat{B}_{i-1,j}^{\iota-1} + \hat{B}_{i+1,j}^{\iota+1} \right), \\ \hat{\kappa}^y &= \frac{\Delta y^2}{2} \left(\hat{B}_{i,j-1}^{\iota-2} + \hat{B}_{i,j+1}^{\iota+2} \right).\end{aligned}\quad (7)$$

Iterating equation (7) for all M locations yields a complete estimate of \mathbf{K} . Following Nummelin et al. (2018) we do not apply the method at boundary locations or impose any boundary conditions. The 5-point stencil does not provide the off-diagonal components of \mathbf{K} and we simply assume that they are zero. Therefore, in regions where the diffusion ellipse is not aligned with the Cartesian grid and the eccentricity of the diffusivity ellipse is high, we underestimate the magnitude of \mathbf{K} . In future, one could alleviate this issue by aligning the local stencil with the orientation of the local correlation ellipse (Lumpkin and Johnson 2013).

MicroInverse provides a statistical estimate of diffusivity that is independent of the underlying processes that contribute to the sub-gridscale tracer transport. These processes cause an initial tracer anomaly to spread to its surroundings and MicroInverse provides a statistical measure of the spreading rate. In this manuscript we use theory to separate these processes into transport by sub-gridscale velocity fluctuations and by large scale shear and

strain (see sections 2.a-b, respectively). In the rest of the manuscript we adopt the following terminology:

- We use *sub-gridscale* for scales that are smaller than the MicroInverse stencil size (Fig. 1) and *sub-gridscale stirring* for tracer transport by sub-gridscale velocity fluctuations.
- We use *shear* for the tracer transport by large scale shear dispersion.
- We use *mixing* and *diffusion* as a generic terms for tracer spreading without any assumption about the underlying process causing it.

Here we choose to use *sub-gridscale stirring* instead of, for example, *sub-gridscale mixing*, because physically the sub-gridscales considered in this study are still dominated by stirring by mesoscale eddies. The *sub-gridscale stirring* appears as diffusion when diagnosed with MicroInverse at coarser resolution.

b. Diffusivity and the Kinetic Energy Spectra

To understand the scale dependence of diffusivity in a broader context, we shortly review the theory linking the diffusivity to the Kinetic Energy Spectra. A large part of modern mesoscale eddy parameterizations, and our understanding of mixing, relies on the mixing length theory, (2). The mixing length theory itself is based on a concept of turbulent diffusion in which a tracer is mixed by velocity fluctuations with a characteristic length scale l_{eddy} .

Depending on the assumptions of underlying kinetic energy spectra one can derive different diffusivity-length scale relations. Within the *energy inertial subrange*, the kinetic energy spectrum has the form $KE = \varepsilon^{2/3} l^{5/3}$ where l is an inverse wavenumber and ε is the kinetic energy flux in wavenumber space (constant within the subrange). Noting that $u_{rms} = \sqrt{\frac{\partial KE}{\partial l}}$

and substituting to (2) gives

$$\kappa \sim \varepsilon^{1/3} l^{4/3}. \quad (8)$$

Within the *enstrophy inertial subrange*, which corresponds to the non-local regime of relative-dispersion (Bennett 1984), stirring is dominated by the large scale flow. The kinetic energy spectrum takes the form $KE = \nu^{2/3} l^3$ where ν is the enstrophy flux (constant within the subrange; Z is enstrophy defined as the vorticity variance, i.e. squared curl of the velocity field, $Z = |\nabla \times \mathbf{u}|^2$; Vallis 2006) and substituting to (2) gives

$$\kappa \sim \nu^{1/3} l^2. \quad (9)$$

In more general terms $n > 1$ simply implies that there is more kinetic energy available for mixing at larger spatial scales. One expects to find $n > 1$ at small length scales, but to drop below 1 as the length scale grows beyond the locally dominating scale of flow and diffusivity approaches a constant.

It is also worth noting that equations (8) and (9) are based on dimensional arguments and therefore they do not provide unique solutions. For example, Bennett (1984, 1987) argues that the exponential growth of particle separation, that has been used to argue for the enstrophy inertial subrange (eq. 9; Ollitrault et al. 2005; Vallis 2006), is achieved whenever the kinetic energy spectrum is proportional to l^n and $n \geq 3$. Similarly, Okubo (1971) and Bennett (1987) show that shear flow leads to a $l^{4/3}$ diffusivity scaling, and thus the presence of a $4/3$ exponent does not necessarily indicate an energy inertial subrange. In realistic ocean different flow regimes are expected to co-exist and therefore we do not expect to see a clear evidence of any theoretically predicted diffusivity-length scale relationship in our time mean estimates of the surface ocean diffusivity.

In the remainder of this paper, with the above caveats in mind, we will use the length scale dependence of the MicroInverse estimates together with theoretical estimates (see section 4.c) to gain insight into the processes underlying the diagnosed diffusivities.

3. Data

A detailed description of the data products and related data processing can be found in Appendix B, but here we list the main data sources. The MicroInverse diffusivity estimates are based on two data sources: i) the OI-SST (AVHRR only) record for 1982–2017 at 0.25° resolution (Reynolds et al. 2007, see also Banzon and Reynolds (last modified, Jun 16 2018)) ii) a kinematic tracer experiment in an idealized 2D configuration of the MITgcm (Marshall et al. 1997) with a horizontal resolution of 0.1° on a regular latitude/longitude grid for 1993–2017. In section 4.c we also use theoretical estimates of the sub-gridscale stirring and large scale shear-driven mixing that are based on surface ocean velocities at 0.25° resolution from the Copernicus-Globcurrent product (combination of altimeter data with estimated Ekman flow; Rio et al. 2014).

4. Results

We focus on the scale-dependence and spatial distribution of κ . In sections 4.a and 4.b we discuss the MicroInverse based estimates, which we then compare to theory in section 4.c. In the following, subscripts distinguish between sea surface temperature anomaly (SSTA) and idealized tracer simulation (MITgcm) based diffusivities.

a. Spatial Structure

Figure 2a shows that κ_{SSTA} at 0.5° resolution peaks in the tropics ($\kappa_{SSTA} \sim 2500 \text{ m}^2 \text{ s}^{-1}$) and around the boundary currents ($\kappa_{SSTA} \sim 1500 \text{ m}^2 \text{ s}^{-1}$), whereas minima are found on the eastern flanks of the subtropical gyres ($\kappa_{SSTA} \sim 100 \text{ m}^2 \text{ s}^{-1}$). This pattern is the same for κ_{MITgcm} (Fig. 2b-c), but diffusivities are weaker than κ_{SSTA} outside the tropics. κ_{MITgcm} peaks at $\sim 1000 \text{ m}^2 \text{ s}^{-1}$ in the boundary currents. There are also large areas where κ_{MITgcm} is below $250 \text{ m}^2 \text{ s}^{-1}$, with minimum diffusivities at $\mathcal{O}(10) \text{ m}^2 \text{ s}^{-1}$ (values below the model grid scale diffusivity of $25 \text{ m}^2 \text{ s}^{-1}$ are not reliable).

The peak diffusivities are generally co-located with regions of high kinetic energy (red contours in Fig. 2a-c). We do not expect any diffusivity suppression by the mean flow because we consider diffusivity magnitude and not the across stream diffusivity (see Appendix A and Ferrari and Nikurashin 2010; Abernathey et al. 2010; Klocker et al. 2012a).

Despite the broadly similar spatial patterns, κ_{SSTA} is $\sim 300 \text{ m}^2 \text{ s}^{-1}$ larger than κ_{MITgcm} in the midlatitudes. We relate this difference to the mixing process behind our diffusion estimates. Diffusion of temperature anomalies involves the modification of the temperature field by the velocity field (specifically, by the so called eddy-swirl component due to a phase shift between tracer and sea level anomalies, not by coherent advection of eddies; Hausmann and Czaja 2012; Villas Boas et al. 2015; Amores et al. 2016; Abernathey and Haller 2018). For such modification to happen, there needs to be an eddy velocity component across the temperature contours.

The idealized tracer experiments advect the temperature tracer with geostrophic velocities. Therefore, lateral tracer mixing can only take place if the the sea level field (that sets the geostrophic velocity field) and the surface temperature field are misaligned with each

other (Rhines and Young 1983). In addition to the geostrophic motions, the observed sea surface temperature can be modified by ageostrophic motions. Therefore the difference between κ_{SSTA} and κ_{MITgcm} could be due to at least the following two reasons: (i) The simulated tracer is closely aligned with the mean currents, because it is restored towards the annual mean surface temperature field and the altimetry based velocity fields that drive the simulations are geostrophic and lack variability at short timescales (not shown). We suggest that the restoring suppresses especially the large scale variability - we will discuss this in the next section. (ii) Ageostrophic motions, vertical mixing in the ocean, and small scale mixing in the atmosphere (via air-sea heat exchange) might enhance the diagnosed κ_{SSTA} (note that the large scale atmospheric signals have been removed by spatial filtering; Nummelin et al. 2018). None of these processes operate in the tracer simulations.

b. Scale Dependence

Diffusion is used in models to parameterize the sub-gridscale tracer transport. We expect a relationship between diffusivity and model grid size because the grid size limits the size of the resolved scales, and therefore the intensity of the sub-gridscale stirring and large scale shear. As mentioned in section 1, dimensional arguments suggest that the diffusivity depends on a length scale ($\kappa \propto l^n$).

Figure 3 shows the diffusivity estimates as a function of the effective MicroInverse grid size in the major ocean basins in both hemispheres (see figure caption for details) and Table 2 collects the exponents in the 40-200km range in the same regions. κ_{SSTA} shows $1.22 < n < 1.54$ in the 40-200km range (90% confidence) and $n \geq 1$ scaling for $60\text{km} \leq l \leq 1000\text{km}$ in the tropics. The magnitudes range from $\mathcal{O}(10^3)$ $\text{m}^2 \text{ s}^{-1}$ at $l \sim 60\text{km}$ to $\mathcal{O}(10^5)$ $\text{m}^2 \text{ s}^{-1}$ at $l \sim 1000\text{km}$. In the midlatitudes $n < 1$ for $40\text{km} \leq l \leq 200\text{km}$ and averaging

over the 30°-40° latitude band in both hemispheres gives $0.58 < n < 0.87$ (90% confidence, Fig. S1). The magnitudes range from $\sim 500 \text{ m}^2 \text{ s}^{-1}$ at $l \sim 40\text{km}$ to $\sim 1000 \text{ m}^2 \text{ s}^{-1}$ at $\sim 200\text{km}$. The extra-tropical regions show some increase in n for $l > 400\text{km}$, with diffusivity magnitude peaking at $\mathcal{O}(10^4) \text{ m}^2 \text{ s}^{-1}$ at $l \sim 900\text{km}$. The extra-tropical increase in n at large l is most likely due to the large scale shear related to the boundary currents. κ_{MITgcm} show less difference between the tropics and the extra-tropics, with $1.02 < n < 1.18$ (90% confidence; Table 2) in the tropics and $0.8 < n < 0.93$ in the midlatitudes (90% confidence; Table S1 and Fig. S1) for $40\text{km} < l < 200\text{km}$.

A closer look at the spatial structure of the exponent n for $40\text{km} \leq l \leq 200\text{km}$ (Fig. 4) reveals that the regions with $n > 1$ are found not only in the tropics but also near boundary currents (especially along the Antarctic Circumpolar Current and the Gulf Stream/North Atlantic current). Regions where $n < 1$ are found in the gyre interiors, specifically in the eastern flanks of the subtropical gyres. These results are consistent with the underlying scales of motion: in the tropics and around boundary currents there are flow structures up to $\mathcal{O}(1000)\text{km}$ scale (e.g. jets, jet meanders, and tropical instability waves), whereas in the gyre interiors the largest flow structures are the mesoscale eddies that are limited in size by the local deformation radius of $\mathcal{O}(100)\text{km}$. In the tropics and around boundary currents the diffusivity can increase with length scale beyond the local eddy scale because of the shear/strain associated with large scale flow. In the absence of the large scale flow, the diffusivity increase with l flattens out at scales larger than the eddy scale. Therefore, there is little increase in the diffusivity (n is small) above the local eddy length scale in the gyre interiors (Fig 4; see also supplementary figure S2 and the next section).

c. Mechanistic interpretation of diagnosed diffusivity

To gain insight into space and scale dependence of the surface diffusivity estimates, we consider two effects that contribute to the sub-gridscale tracer transport: sub-gridscale stirring (magnitude denoted by κ_s ; defined in Appendix B.a), and two formulations of large scale shear (magnitudes denoted by κ_{l1} and κ_{l2} ; both defined in Appendix B.b).

In the extra-tropics, both the sub-gridscale stirring and the large scale shear have spatial structure that is qualitatively similar to the spatial structure of κ_{SSTA} and κ_{MITgcm} at 0.5° scale (Fig. 5). Diffusivity is high in the western boundary currents, but small in the eastern subtropical gyres. However, only when integrating the large scale shear over all length scales (κ_{l2}) can we explain the tropical peak in κ_{SSTA} and κ_{MITgcm} (Fig. 6). In contrast, both sub-gridscale stirring (κ_s) and grid scale shear (κ_{l1}) fail to explain the peak because both the kinetic energy and shear are weak at ~ 40 km scale.

In terms of length scale dependence (slope n) between $40\text{km} \leq l \leq 200\text{km}$, all the theoretical estimates also distinguish between the tropics (large n) and midlatitudes (small n ; Figures 7 and 8; compare to empirical estimates in Figs. 3 and 4). However κ_{l1} and κ_s produce results that are closest to κ_{SSTA} scaling (Figs. 7b and 8b,d). Because κ_{l2} is based on an integral formulation of κ_{l1} its length scale dependence is weaker than that of κ_{l1} by definition (Figs. 7c and 8c,d).

So far, the results have pointed towards the importance of the shear driven mixing over sub-gridscale stirring, at least in the tropics. To further examine their relative contributions we use their linear combination:

$$\kappa_{s,l}(h) = b_1\kappa_s(h) + b_2\kappa_l(h), \quad (10)$$

where b_1 and b_2 are the dimensionless parameters κ_l is the magnitude of the large scale shear-driven mixing as defined either in (C3) or (C4). We sweep over the (b_1, b_2) parameter space and compare κ_{MITgcm} to $\kappa_{s,l}$ at 0.5° and 2.5° resolutions, in the tropics (15°S - 15°N) and the midlatitudes (between 15° and 60° in both hemispheres), separately. Figure 9 shows the comparison using three different metrics: The background color shows a mean absolute percentage error ($MAPE = \langle (|\kappa_{MITgcm} - \kappa_{s,l}|) / \kappa_{MITgcm} \rangle$) where the angle brackets denote spatial average; black and white contours are measures of linear correlation; the black contours show the linear least-squares regression slope and the white contours show the squared Pearson correlation coefficient (i.e. degree of spatial variance explained similar to Fig. 6; See Figure S3 for comparison to κ_{SSTA}). The optimal (b_1, b_2) space is found where MAPE is small, the regression slope is one, and the squared Pearson correlation coefficient is high (thick red ellipses show qualitatively where such optima is found). The thin red lines illustrate the ratio between the large scale shear-driven mixing and the sub-gridscale stirring.

The optimum (red ellipse: highest correlation, low MAPE distance and slope ~ 1) at the 0.5° scale is found when the shear driven mixing dominates, both in the tropics and in the midlatitudes (Figure 9 and Fig. S3a; panels a, c, e, g). In general (10) explains at most $\sim 40\%$ ($\sim 30\%$) of the κ_{MITgcm} pattern in the tropics (midlatitudes). The combination of κ_{l1} and κ_s forms a notable exception in the tropical band as both κ_{l1} and κ_s fail to reproduce the κ_{MITgcm} pattern (Fig. 9). At larger scales, we expect that the sub-gridscale stirring better explains the diagnosed diffusivities because a larger part of the kinetic energy spectra becomes sub-gridscale. At 2.5° scale the optima are found when both shear and sub-gridscale stirring have close to equal contribution to $\kappa_{s,l}$, which explains at most $\sim 50\%$ ($\sim 40\%$) of the κ_{MITgcm} pattern in the tropics (midlatitudes; Fig. 9 panels d and h). None

of the theoretical formulations tested here provide a complete description of the diagnosed diffusivities. However, the results do suggest that large scale shear dominates the tracer diffusion at $\sim 40\text{km}$ scale in the tropics, whereas at larger scales and in the midlatitudes, both sub-gridscale stirring and large scale shear are important.

5. Summary and Discussion

We present empirical, tracer based, diffusivity estimates at the ocean surface that vary in space and depend on the scales of motion. We find that sea surface temperature based diffusivity is high ($\mathcal{O}(1000)\text{m}^2\text{s}^{-1}$) in the tropics and around boundary currents, and weak in the eastern side of the subtropical gyres ($\mathcal{O}(100)\text{m}^2\text{s}^{-1}$). The results show a power-law dependence between the estimated diffusivities and scale at which the diffusivity is estimated. In the 40–200km range, we find that the exponent n is between 1.22–1.54 (90% confidence; Table 2) in the tropics, peaks at values above 1 in the boundary currents, and is $0.58 < n < 0.87$ (90% confidence; Table S1) in the midlatitudes. Because the tropics and the boundary currents are 1) characterized by strong shear flow 2) not well characterized by 3-dimensional isotropic turbulence, we suggest that the observed n is due to shear flow and not due to the energy-inertial subrange even if broadly consistent with the $n \sim 4/3$ scaling. This conclusion is in agreement with Okubo (1971) and Bennett (1987) who demonstrated that $n \sim 4/3$ is expected also in shear flow. Further support for the importance of shear comes from a direct comparison between the diagnosed diffusivities and theoretical diffusivity estimates: we find that the spatial patterns of tracer diffusivity and the sea surface temperature diffusivity in the tropics are best explained by large scale shear at 50 km grid size (Fig. 9). On larger scales, and at midlatitudes, eddies are small compared to the grid size and sub-gridscale stirring can explain a larger part of the diagnosed

diffusivities. Figure 10 illustrates these results and their relation to the background processes - thus summarizing our main results.

Our main results can also be seen from the perspective of the local and non-local dispersion regimes recognized in the literature (Eckart 1948; Bennett 1984, 1987; Garrett 2006, and references therein). In the non-local regime, the tracer dispersion is dominated by the large scale shear which separates a tracer patch into long streaks before the cross-streak diffusion homogenizes the tracer field. The local regime is dominated by eddies that are of the size of the tracer patch, and the tracer field is rapidly homogenized. Our results suggest that the non-local regime dominates in the tropics as the integral formulation of the large scale stirring (C4) best reproduces the estimated diffusivities. In the midlatitudes, both regimes are present and our results suggest that both could play an important role in the sub-gridscale mixing. However, other studies, suggest that the large scale flow (i.e. non-local regime) dominates Lagrangian dispersion (and diffusivity) at least over the Gulf Stream (Poje et al. 2010) and the Antarctic Circumpolar Current (Balwada et al. 2019, in review).

The qualitative results arising from this study are robust: the conclusions are similar in two different data-sets and across the ensemble covering several time intervals. However, quantitatively, the results are sensitive to at least two main factors which we summarize here. (i) Seasonality. The results presented here are time mean estimates over several years. However, in many regions, the mesoscale activity changes seasonally (e.g. Busecke et al. 2017; Ducet et al. 2000) and we expect that the diffusivity magnitudes and the length scale dependence would change if estimated with data from a single season only. (ii) Off-diagonal components of the diffusion tensor. In regions where the diffusion tensor is not aligned with the Cartesian latitude-longitude grid and the eccentricity of the diffusivity ellipse is high, we underestimate the magnitude of the tensor. We expect that the underestimation is most

pronounced in regions of western boundary currents that are often aligned in $\sim 45^\circ$ angle to the Cartesian grid (see also Appendix A).

The diffusivity estimates presented in this paper are based on the spatial covariance properties of a tracer field and the methodology can be applied to any two-dimensional scalar field. For example, the MicroInverse method could be applied to tracers or layer thickness on isopycnal coordinates which would lead to estimates that are directly relevant for the widely adopted Gent & McWilliams and Redi (GM-Redi) eddy parameterization (Redi 1982; Gent and McWilliams 1990; Gent et al. 1995; Gent 2011). However, in addition to estimating the diffusion tensor, there are other challenges to the sub-gridscale mixing parameterizations; (i) The tracer transport in the GM-Redi-framework depends not only on the diffusion tensor, but also on the slope of the neutral surface which is challenging to estimate (for recent advances, see Groeskamp et al. 2019). (ii) Models are known to be sensitive to how the GM-Redi-framework is applied in the surface mixed layer, where the isopycnals outcrop and can be vertically oriented (Danabasoglu et al. 2008; Farneti et al. 2015). We envision that diagnosing surface and subsurface (along isopycnal) diffusivities using MicroInverse could provide guidance on how this transformation can be done in the existing parameterizations (Griffies 2004; Ferrari et al. 2008, 2010; Mak et al. 2018). (iii) In most practical implementations of the GM-Redi-framework the advective and diffusive parts of the full diffusion tensor (\mathbf{K}_t) are described by the same diffusion coefficient (Griffies 1998). MicroInverse could be used to estimate the two coefficients and quantify their relation given suitable data. (iv) Most present-day mesoscale eddy parameterizations take the mixing length theory (eq. 2) as their starting point, similar to the sub-gridscale stirring estimate used in section 4c. However, in most model implementations the eddy energy is estimated using Eady theory, although parameterizations that carry prognostic eddy energy

equation are developing (Mak et al. 2018; Jansen et al. 2019; Bachman 2019). Introducing Eady growth rate (σ ; Vallis 2006) to mixing length theory gives $\kappa \sim \sigma l^2$ (where l is a length scale; see e.g. Eden et al. 2009, for a comparison of a few different implementations) and links the diffusivity to stratification in these parameterizations. However, our results emphasize the role of shear driven mixing (Le Sommer et al. 2011) that is able to explain a large part ($> 50\%$, in the tropics; $> 30\%$ in the midlatitudes) of the spatial variability of the diagnosed diffusivity magnitude (see also Poje et al. 2010; Balwada et al. 2019, in review). Originally, Le Sommer et al. (2011) derived the theory of shear driven mixing for mesoscale resolving models, but our results suggest that such a parameterization should be used also in coarser resolution models.

In addition to the shear, the fact that κ_{MITgcm} is generally smaller than κ_{SSTA} and has weaker length-scale dependence, suggests that processes not considered in present-day eddy-parameterizations can be important for lateral tracer mixing. We suggest that the difference follows from the sea surface temperature based diffusivities being enhanced by small scale processes (such as air-sea interaction or sub-mesoscale motions) and the idealized tracer being closely aligned with the velocity field. This close alignment is due to a combination of factors including the relatively coarse resolution of the underlying altimetry based velocity field and the tracer restoring to initial conditions at monthly timescale.

Acknowledgments. AN would like to thank Anand Gnanadesikan for useful discussions and comments on ocean mixing. AN and TWNH thank the NSF Directorate for Geosciences (grant number 1536554) for financial support. AN also acknowledges support from NORCE to finalize the manuscript. This study has been conducted using E.U. Copernicus Marine Service Information. NOAA High Resolution SST data

(NOAA OISST) is provided by the NOAA/OAR/ESRL PSD, Boulder, Colorado, USA, from their Web site at <https://www.esrl.noaa.gov/psd/>. The Mesoscale Eddy Trajectory Atlas products were produced by SSALTO/DUACS and distributed by AVISO+ (<http://www.aviso.altimetry.fr/>) with support from CNES, in collaboration with Oregon State University with support from NASA. The data and further details are available at <https://www.aviso.altimetry.fr/en/data/products/value-added-products/global-mesoscale-eddy-trajectory-product.html>. We thank the anonymous reviewers for constructive comments that lead to a much improved the manuscript, and the editor, Joe LaCasce, for helpful suggestions.

Data availability statement. The satellite data used in this study is freely available: OISST from <https://psl.noaa.gov/data/gridded/data.noaa.oisst.v2.highres.html> and the Eddy Trajectory Atlas from <https://www.aviso.altimetry.fr/en/data/products/value-added-products/global-mesoscale-eddy-trajectory-product.html>. The tracer simulation is available through the corresponding author: aleksi.h.nummeli@gmail.com. The code to reproduce the results is available at <https://doi.org/10.5281/zenodo.4126315> and subset of the horizontal diffusivities is available at <https://doi.org/10.5281/zenodo.4106563>.

APPENDIX A

Effect of Strong Mean Flow on the Diffusivity Tensor

Here we illustrate the effect of a strong mean flow on the diffusivity tensor \mathbf{K} . We demonstrate that it does not change the magnitude of diffusivity, but it elongates the diffusion ellipse along the flow direction and squeezes it in the cross stream direction.

Begin with the along stream diffusivity. Taylor (1953) and Aris (1956) suggest that shear dispersion enhances the along stream diffusivity (originally derived for pipeflow). Taking the diffusivity to be half the growth rate of the tracer variance, Aris (1956, see their equation (41), note the slightly different notation) arrives at

$$\kappa_{along} = \kappa_m \left(1 + a_0 \frac{U^2 L^2}{\kappa_m^2} \right), \quad (\text{A1})$$

where κ_{along} is the shear-enhanced along stream diffusivity, κ_m is the mean along stream diffusivity over the pipe cross-section, a_0 is a constant ($a_0 \ll 1$), which in the pipe flow depends on the pipe geometry, U is the velocity scale, and L is a length scale. In the pipe flow U and L are the maximum velocity and the diameter of the pipe, respectively. Combining (A1) with the mixing length theory, i.e. $\kappa_m \sim u_{rms} l$, and assuming that the length scales l and L are the same (or linearly related) we can write

$$\kappa_{along} = \kappa_m \left(1 + a_1 \frac{U^2}{u_{rms}^2} \right), \quad (\text{A2})$$

where a_1 is a constant. This theory was derived for pipe flow, but it has been applied in the ocean to explain horizontal mixing enhanced by the vertical shear (e.g., Young et al. 1982, and references therein).

Now consider the across stream diffusivity. Ferrari and Nikurashin (2010) discuss the suppression of across stream diffusivity in the Southern Ocean by the mean flow. They use a stochastic surface quasi-geostrophic model and take the across stream diffusivity to be the ratio between across stream tracer flux and across stream tracer gradient (for which they derive analytical expressions in their model). They relate eddy phase speed to the mean current speed, eddy decorrelation time scale to eddy strain rate, and assume isotropic turbulence, which allows them to express the across-stream diffusivity κ_{across} as (see their

equation 17, and note again the slightly different notation)

$$\kappa_{across} = \frac{\kappa_0}{\left(1 + a_2 \frac{U_0^2}{u_{rms}^2}\right)}, \quad (\text{A3})$$

where a_2 is a constant and κ_0 is the diffusivity without the mean flow U_0 .

The two theories suggest that the mean flow enhances the along stream diffusivity, but suppresses the across stream diffusivity. Taking $\kappa_0 = a_3 u_{rms} l$ and assuming that $\kappa_0 = \kappa_m$, $U = U_0$, and $a_3 = a_2 = a_1$, we see that (A2) and (A3) are related by the same scaling factor:

$$\begin{aligned} \kappa_{along} &= \kappa_0 \left(1 + a_1 \frac{U^2}{u_{rms}^2}\right) \\ \kappa_{across} &= \kappa_0 \left(1 + a_1 \frac{U^2}{u_{rms}^2}\right)^{-1}. \end{aligned} \quad (\text{A4})$$

Although simplifying assumptions (Aris 1956; Ferrari and Nikurashin 2010) are required to reach (A4), the result is important and enlightening: (A4) indicates that the mean flow does not modify the diffusivity magnitude ($\sqrt{\kappa_{along}\kappa_{across}} = \kappa_0$ i.e., the area of the diffusion ellipse is preserved). Instead, it elongates the diffusion ellipses along the flow direction and contracts them across it.

APPENDIX B

Data sources and processing

a. Data sources

For the best results, the MicroInverse methodology requires long relatively high-time resolution gridded timeseries (Nummelin et al. 2018). Satellite-based data are well suited for the purpose which is why we use the global sea surface temperature anomalies from the OI-SST (AVHRR only) record for 1982–2017 at 0.25° resolution (Reynolds et al. 2007, see also Banzon and Reynolds (last modified, Jun 16 2018)).

To avoid issues related to sampling and noise in observations, we also diagnose diffusivity from a kinematic tracer experiment in an idealized 2D configuration of the MITgcm (Marshall et al. 1997) with a horizontal resolution of 0.1° on a regular latitude/longitude grid for 1993–2017. The model tracer field is initialized with mean satellite sea surface temperature (based on AMSR-E data; Reynolds et al. 2007) and then prescribed velocities are used to solve the 2D advection-diffusion equation. The passive temperature tracer field relaxes towards the initial conditions with a restoring timescale of one month. The prescribed velocity field is based on an altimetry based velocity field (geostrophic velocities, calculated with β -plane approximation in the tropics; see Rio et al. 2016, for details) that is linearly interpolated from the Aviso 0.25° grid onto the finer model grid and then corrected to be non-divergent following Abernathey and Marshall (2013). As a result, tracer mixing at scales between 0.1° - 0.25° is purely driven by shear and strain in the mesoscale flow field (similar to Le Sommer et al. 2011). We note that the non-divergence correction introduces spurious variability at the basin scale (Busecke and Abernathey 2019), but this does not affect our estimates as we consider smaller scales. The simulation has a constant uniform explicit horizontal sub-grid-scale diffusivity of $25 \text{ m}^2 \text{ s}^{-1}$. All data products have daily time-resolution, although the effective time resolution is lower for the sea surface temperature data (Reynolds et al. 2007) and for the sea level data used to drive the idealized model simulation.

b. Data Processing

The code for reproducing the data processing is available at <https://doi.org/10.5281/zenodo.4126315>.

1) MICROINVERSE ESTIMATES

We define the anomalies at every grid point as departures from the daily averages and we remove any linear trends in time. Since we remove the daily averages, we do not remove seasonality explicitly by, for example, fitting periodic signals. In addition, we remove the large scale mean from the OI-SST data (moving area average of 4×8 latitude-longitude box: the inversion is insensitive to the choice of the filter size; Nummelin et al. 2018) in order to minimize the atmospheric imprint. We perform this step only for OI-SST data because the tracer simulation is free of such atmospheric imprints by construction.

The OI-SST data set is produced from noisy observations with gaps in both space and time using filtering, interpolation, and extrapolation. In order to obtain robust diffusivity estimates from such data we take a Monte-Carlo approach. We split the full timeseries in 30 segments, each 10-years long, and estimate the diffusivity for each segment separately with MicroInverse. Here we focus on the median diffusivity values over the 30 member ensemble. For consistency, we use the same approach with the tracer simulations.

2) SPATIAL FILTERING AND LENGTH SCALES

The scale dependent estimates of κ are based on temperature and tracer fields that are regridded to coarser resolutions using first order conservative remapping (Ramshaw 1985) as implemented in the EMSF software (Coquart and Valcke 2020) and in its higher level interface, the `xesmf` python package (Zhuang et al. 2020). The results are then regridded to a common 2° grid and the scale dependence is estimated from a linear fit in log-log space (the choice of the common grid-scale does not affect the main results). Because MicroInverse uses a 5-point stencil to estimate the diffusivity, the nominal length scale of these estimates is twice the grid size of the dataset from which the diffusivity is estimated (Fig. 1).

To implement (C2) and (C4), we low-pass filter the velocity data with a Gaussian filter (following Aluie et al. 2018; Aluie 2018, see Appendix B) and define the small scale velocity field (\mathbf{u}_s) as the residual between the original velocity field (\mathbf{u}) and the low-pass filtered velocity field (\mathbf{u}_l). The smallest filter size (h_0) is 3 by 3 grid cells, which we compare to the MicroInverse diffusivity at 0.5° scale (5-point stencil on a 0.25° grid, see Fig. 1) as they are associated with similar length scales. In section 4.c we also compare the theoretical diffusivity estimates at a 15×15 grid cell filter size and MicroInverse diffusivities at 2.5° resolution.

3) SPATIAL FILTERING OF VELOCITY ON THE SPHERE

Spatial filtering of a vector field on a spherical surface is less straightforward than filtering a scalar field. Following Aluie et al. (2018) and Aluie (2018) we filter the velocity field by first decomposing it into a velocity potential and streamfunction using the Helmholtz-Hodge decomposition. To this end we use the `pyNHHD` python package (Bhatia et al. 2014), which we have modified to accommodate spherical surfaces (modified Python code available at <https://github.com/AleksiNummelin/naturalHHD/tree/spherical>). The decomposition based velocity field has a 5% error compared to the original (not shown), firstly because of the inaccurate estimation of velocity derivatives (with central differences), and secondly due to inaccurate representation of Green's function in the disconnected spherical domain. We then derive the low-pass filtered velocity fields from low-pass filtered streamfunction and velocity potential (using a Gaussian filter). Note that the smallest filter size (full-width-half-maximum of the Gaussian kernel) is three grid cells, essentially the same size as the smallest MicroInverse stencil (Fig. 1).

APPENDIX C

Theoretical diffusivity estimates

a. Sub-gridscale Stirring

We use the mixing length theory to estimate diffusivity by sub-gridscale processes. Mixing length theory is usually applied in the context of a time or an ensemble average (e.g. Klocker and Marshall 2014), but we modify it to account for scale dependence by spatially-filtering observed surface velocity fields (we use the Copernicus-Globcurrent product, see section 2.5 and Appendix b). We define a scale-dependent root mean square velocity as

$$u_s^{rms}(h) = \sqrt{[u_s(h) - \overline{u_s(h)}]^2 + [v_s(h) - \overline{v_s(h)}]^2}, \quad (C1)$$

where h denotes the scale of the high-pass spatial filter, subscript s denotes the small scale, u and v are the two components of the velocity vector, and the over-bar denotes a time average.

Following mixing length theory (2), one multiplies (C1) with a relevant length scale (Vallis 2006). The naive approach could be to use the filter size h as the length scale. However, because u_s^{rms} becomes (locally) constant when h is larger than the largest eddies, the naive approach would lead to linear scale dependency at large filter sizes. This is clearly unrealistic (see also Canuto et al. 2019). Here we chose the following, ad-hoc, approach and define the relevant length scale to be the minimum of h and the observed eddy radius (L_r from the mesoscale eddy trajectory atlas, Chelton et al. 2011, 1998). Within the 6°S-6°N tropical latitude band, where there are essentially no observed eddies, we use linear interpolation to estimate L_r . The diffusivity by subgrid-scale stirring is then

$$\kappa_s(h) \sim u_s^{rms}(h) \min(h, L_r). \quad (C2)$$

Equation (C2) lacks a dimensionless constant which we tune in section 4.c.

b. Large Scale Shear

Strain in the flow above scale h also leads to tracer transport at scales below h due to stirring (Eckart 1948). To capture this effect Le Sommer et al. (2011) propose the following parametrization based on theory and model simulations:

$$\mathbf{K}_{l1}(h) \equiv \begin{pmatrix} \kappa_{l1}^x & \kappa_{l1}^{xy} \\ \kappa_{l1}^{xy} & \kappa_{l1}^y \end{pmatrix} \sim \frac{h^2}{2} (1 + \delta) \begin{pmatrix} p & \rho \\ \rho & q \end{pmatrix}. \quad (C3)$$

Equation (C3) states that the sub-gridscale diffusivity due to large scale shear is a function of shear strain $\rho = \frac{\partial v_l}{\partial x} + \frac{\partial u_l}{\partial y}$, normal strain $a = \frac{\partial u_l}{\partial x} - \frac{\partial v_l}{\partial y}$, filter size h , and scaled divergence $\delta = \frac{\frac{\partial u_l}{\partial x} + \frac{\partial v_l}{\partial y}}{\sqrt{\rho^2 + a^2}}$. Here u_l and v_l are the two low-pass filtered velocity components. Terms p and q are combinations of the the two strain terms: $p = \sqrt{\rho^2 + a^2} + a$ and $q = \sqrt{\rho^2 + a^2} - a$.

The drawback of (C3) is that the flow properties close to the filter scale h dominate the value of \mathbf{K}_{l1} , which leads to underestimation of stirring by scales much larger than h . This is because divergence, shear, and strain are based on velocity gradients at scale h . To alleviate this issue we also use an *ad-hoc* formulation that integrates over the strain and divergence at different scales:

$$\mathbf{K}_{l2}(h) \equiv \begin{pmatrix} \kappa_{l2}^x & \kappa_{l2}^{xy} \\ \kappa_{l2}^{xy} & \kappa_{l2}^y \end{pmatrix} \sim \int_h^{h_{max}} h [1 + \delta(h')] \begin{pmatrix} p(h') & \rho(h') \\ \rho(h') & q(h') \end{pmatrix} dh', \quad (C4)$$

where h is the filter size, h_{max} is the maximum filter size and h' is the integration variable.

Here, $h_{max} = 15^\circ$ is large enough so that in midlatitudes the magnitude of \mathbf{K}_{l2} is insensitive

to small changes in h_{max} , although in the tropics \mathbf{K}_{l2} is still increasing with h_{max} (not shown).

We show results for the diffusivity magnitude ($\kappa_{l1} = \|\mathbf{K}_{l1}\| = \sqrt{\kappa_{l1}^x \kappa_{l1}^y}$ and $\kappa_{l2} = \|\mathbf{K}_{l2}\| = \sqrt{\kappa_{l2}^x \kappa_{l2}^y}$, from (C3) and (C4), respectively), which we calculate after diagonalising the diffusion tensor (therefore the magnitude is rotation invariant and corresponds to the area of an ellipse defined by the diagonal components). Similar to (C2), we have left out a dimensionless constant also from (C3) and (C4). We tune these constants in section 4.c.

References

- Abernathey, R., D. Ferreira, and A. Klocker, 2013: Diagnostics of isopycnal mixing in a circumpolar channel. *Ocean Modelling*, **72**, 1 – 16, doi:<https://doi.org/10.1016/j.ocemod.2013.07.004>, URL <http://www.sciencedirect.com/science/article/pii/S1463500313001200>.
- Abernathey, R., and G. Haller, 2018: Transport by lagrangian vortices in the eastern pacific. *Journal of Physical Oceanography*, **48** (3), 667–685, doi:10.1175/JPO-D-17-0102.1, URL <https://doi.org/10.1175/JPO-D-17-0102.1>.
- Abernathey, R., J. Marshall, M. Mazloff, and E. Shuckburgh, 2010: Enhancement of Mesoscale Eddy Stirring at Steering Levels in the Southern Ocean. *Journal of Physical Oceanography*, **40** (1), 170–184, doi:10.1175/2009JPO4201.1, URL <https://doi.org/10.1175/2009JPO4201.1>.
- Abernathey, R. P., and J. Marshall, 2013: Global surface eddy diffusivities derived from satellite altimetry. *Journal of Geophysical Research: Oceans*, **118** (2), 901–916, doi:10.1002/jgrc.20066, URL <http://dx.doi.org/10.1002/jgrc.20066>.

- Alexander, M. A., L. Matrosova, C. Penland, J. D. Scott, and P. Chang, 2008: Forecasting Pacific SSTs: Linear Inverse Model Predictions of the PDO. *Journal of Climate*, **21** (2), 385–402, doi:10.1175/2007JCLI1849.1.
- Aluie, H., 2018: Convolutions on the sphere: Commutation with differential operators. *GEM - International Journal on Geomathematics*, **accepted (X)**, X, doi:https://arxiv.org/abs/1808.03323v2, URL https://arxiv.org/abs/1808.03323v2.
- Aluie, H., M. Hecht, and G. K. Vallis, 2018: Mapping the energy cascade in the north atlantic ocean: The coarse-graining approach. *Journal of Physical Oceanography*, **48** (2), 225–244, doi:10.1175/JPO-D-17-0100.1, URL https://doi.org/10.1175/JPO-D-17-0100.1.
- Amores, A., O. Melnichenko, and N. Maximenko, 2016: Coherent mesoscale eddies in the north atlantic subtropical gyre: 3-d structure and transport with application to the salinity maximum. *Journal of Geophysical Research: Oceans*, **122** (1), 23–41, doi:10.1002/2016JC012256, URL https://agupubs.onlinelibrary.wiley.com/doi/abs/10.1002/2016JC012256.
- Aris, R., 1956: On the dispersion of a solute in a fluid flowing through a tube. *Proceedings of the Royal Society of London A: Mathematical, Physical and Engineering Sciences*, **235** (1200), 67–77, doi:10.1098/rspa.1956.0065, URL http://rspa.royalsocietypublishing.org/content/235/1200/67.
- Armi, L., and H. Stommel, 1983: Four views of a portion of the north atlantic subtropical gyre. *Journal of Physical Oceanography*, **13** (5), 828–857, doi:10.1175/1520-0485(1983)013<0828:FVOAPO>2.0.CO;2.

- Bachman, S., and B. Fox-Kemper, 2013: Eddy parameterization challenge suite. I: Eady spindown. *Ocean Modelling*, **64**, 12–28, doi:10.1016/j.ocemod.2012.12.003, URL <http://dx.doi.org/10.1016/j.ocemod.2012.12.003>.
- Bachman, S., B. Fox-Kemper, and F. O. Bryan, 2015: A tracer-based inversion method for diagnosing eddy-induced diffusivity and advection. *Ocean Modelling*, **86**, 1–14, doi:10.1016/j.ocemod.2014.11.006, URL <http://dx.doi.org/10.1016/j.ocemod.2014.11.006>.
- Bachman, S., D. Marshall, J. Maddison, and J. Mak, 2017a: Evaluation of a scalar eddy transport coefficient based on geometric constraints. *Ocean Modelling*, **109**, 44 – 54, doi:10.1016/j.ocemod.2016.12.004, URL <https://doi.org/10.1016/j.ocemod.2016.12.004>.
- Bachman, S. D., 2019: The GM+E closure: A framework for coupling backscatter with the Gent and McWilliams parameterization. *Ocean Modelling*, **136**, 85 – 106, doi:<https://doi.org/10.1016/j.ocemod.2019.02.006>, URL <http://www.sciencedirect.com/science/article/pii/S1463500318301975>.
- Bachman, S. D., B. Fox-Kemper, and F. O. Bryan, 2020: A diagnosis of anisotropic eddy diffusion from a high-resolution global ocean model. *Journal of Advances in Modeling Earth Systems*, **12** (2), e2019MS001904, doi:10.1029/2019MS001904, URL <https://agupubs.onlinelibrary.wiley.com/doi/abs/10.1029/2019MS001904>.
- Bachman, S. D., B. Fox-Kemper, and B. Pearson, 2017b: A scale-aware subgrid model for quasi-geostrophic turbulence. *Journal of Geophysical Research: Oceans*, **122** (2), 1529–1554, doi:10.1002/2016JC012265, URL <https://agupubs.onlinelibrary.wiley.com/doi/abs/10.1002/2016JC012265>.

- Balwada, D., J. H. LaCasce, K. Speer, and R. Ferrari, 2019, in review: Relative Dispersion in the Antarctic Circumpolar Current. *Journal of Physical Oceanography*, **49** (5), 1141–1157, doi:<https://doi.org/10.31223/osf.io/mhtsb>.
- Bennett, A. F., 1984: Relative dispersion: Local and nonlocal dynamics. *Journal of the Atmospheric Sciences*, **41** (11), 1881–1886, doi:10.1175/1520-0469(1984)041<1881:RDLAND>2.0.CO;2, URL [https://doi.org/10.1175/1520-0469\(1984\)041\(1881:RDLAND\)2.0.CO;2](https://doi.org/10.1175/1520-0469(1984)041(1881:RDLAND)2.0.CO;2).
- Bennett, A. F., 1987: A lagrangian analysis of turbulent diffusion. *Reviews of Geophysics*, **25** (4), 799–822, doi:10.1029/RG025i004p00799, URL <https://agupubs.onlinelibrary.wiley.com/doi/abs/10.1029/RG025i004p00799>.
- Bhatia, H., V. Pascucci, and P. Bremer, 2014: The natural helmholtz-hodge decomposition for open-boundary flow analysis. *IEEE Transactions on Visualization and Computer Graphics*, **20** (11), 1566–1578, doi:10.1109/TVCG.2014.2312012.
- Bracco, A., J. Choi, J. Kurian, and P. Chang, 2018: Vertical and horizontal resolution dependency in the model representation of tracer dispersion along the continental slope in the northern gulf of mexico. *Ocean Modelling*, **122**, 13 – 25, doi:<https://doi.org/10.1016/j.ocemod.2017.12.008>, URL <http://www.sciencedirect.com/science/article/pii/S1463500317302123>.
- Busecke, J., R. P. Abernathey, and A. L. Gordon, 2017: Lateral eddy mixing in the subtropical salinity maxima of the global ocean. *Journal of Physical Oceanography*, **47** (4), 737–754, doi:10.1175/JPO-D-16-0215.1, URL <https://doi.org/10.1175/JPO-D-16-0215.1>.

- Busecke, J. J. M., and R. P. Abernathey, 2019: Ocean mesoscale mixing linked to climate variability. *Science Advances*, **5** (1), doi:10.1126/sciadv.aav5014, URL <http://advances.sciencemag.org/content/5/1/eaav5014>.
- Canuto, V. M., Y. Cheng, A. M. Howard, and M. S. Dubovikov, 2019: Three-dimensional, space-dependent mesoscale diffusivity: Derivation and implications. *Journal of Physical Oceanography*, **49** (4), 1055–1074, doi:10.1175/JPO-D-18-0123.1, URL <https://doi.org/10.1175/JPO-D-18-0123.1>, <https://doi.org/10.1175/JPO-D-18-0123.1>.
- Chelton, D. B., R. A. deSzoeke, M. G. Schlax, K. El Naggar, and N. Siwertz, 1998: Geographical variability of the first baroclinic rossby radius of deformation. *Journal of Physical Oceanography*, **28** (3), 433–460, doi:10.1175/1520-0485(1998)028<0433:GVOTFB>2.0.CO;2, URL [https://doi.org/10.1175/1520-0485\(1998\)028<0433:GVOTFB>2.0.CO;2](https://doi.org/10.1175/1520-0485(1998)028<0433:GVOTFB>2.0.CO;2).
- Chelton, D. B., M. G. Schlax, and R. M. Samelson, 2011: Global observations of nonlinear mesoscale eddies. *Progress in Oceanography*, **91** (2), 167 – 216, doi:10.1016/j.pocean.2011.01.002, URL <https://doi.org/10.1016/j.pocean.2011.01.002>.
- Cole, S. T., C. Wortham, E. Kunze, and W. B. Owens, 2015: Eddy stirring and horizontal diffusivity from argo float observations: Geographic and depth variability. *Geophysical Research Letters*, **42** (10), 3989–3997, doi:10.1002/2015GL063827.
- Coquart, L., and S. Valcke, 2020: ESMF v7.1.0r remapping between two structured grids and between two unstructured grids and one structured grid. Zenodo, URL <https://doi.org/10.5281/zenodo.3903387>, doi:10.5281/zenodo.3903387.
- Danabasoglu, G., R. Ferrari, and J. C. McWilliams, 2008: Sensitivity of an ocean general circulation model to a parameterization of near-surface eddy fluxes. *Journal of Cli-*

mate, **21** (**6**), 1192–1208, doi:10.1175/2007JCLI1508.1, URL <https://doi.org/10.1175/2007JCLI1508.1>, <https://doi.org/10.1175/2007JCLI1508.1>.

Deser, C., M. A. Alexander, and M. S. Timlin, 2003: Understanding the persistence of sea surface temperature anomalies in midlatitudes. *Journal of Climate*, **16** (**1**), 57–72, doi:10.1175/1520-0442(2003)016<0057:UTPOSS>2.0.CO;2.

Ducet, N., P. Y. Le Traon, and G. Reverdin, 2000: Global high-resolution mapping of ocean circulation from topex/poseidon and ers-1 and -2. *Journal of Geophysical Research: Oceans*, **105** (**C8**), 19 477–19 498, doi:10.1029/2000JC900063, URL <https://agupubs.onlinelibrary.wiley.com/doi/abs/10.1029/2000JC900063>.

Eckart, C., 1948: An analysis of the stirring and mixing processes in incompressible fluids. *jmr*, **7**, 265–275.

Eden, C., M. Jochum, and G. Danabasoglu, 2009: Effects of different closures for thickness diffusivity. *Ocean Modelling*, **26** (**1**), 47 – 59, doi:<https://doi.org/10.1016/j.ocemod.2008.08.004>, URL <http://www.sciencedirect.com/science/article/pii/S1463500308001261>.

Farneti, R., and Coauthors, 2015: An assessment of antarctic circumpolar current and southern ocean meridional overturning circulation during 1958–2007 in a suite of interannual core-ii simulations. *Ocean Modelling*, **93**, 84 – 120, doi:<https://doi.org/10.1016/j.ocemod.2015.07.009>.

Ferrari, R., S. M. Griffies, A. G. Nurser, and G. K. Vallis, 2010: A boundary-value problem for the parameterized mesoscale eddy transport. *Ocean Modelling*, **32** (**3**), 143 – 156, doi:<https://doi.org/10.1016/j.ocemod.2010.01.004>, URL <http://www.sciencedirect.com>.

com/science/article/pii/S1463500310000065, the magic of modelling: A special volume commemorating the contributions of Peter D. Killworth – Part 2.

Ferrari, R., J. C. McWilliams, V. M. Canuto, and M. Dubovikov, 2008: Parameterization of eddy fluxes near oceanic boundaries. *Journal of Climate*, **21** (12), 2770–2789, doi:10.1175/2007JCLI1510.1, URL <https://doi.org/10.1175/2007JCLI1510.1>.

Ferrari, R., and M. Nikurashin, 2010: Suppression of eddy diffusivity across jets in the southern ocean. *Journal of Physical Oceanography*, **40** (7), 1501–1519, doi:10.1175/2010JPO4278.1.

Fox-Kemper, B., and Coauthors, 2019: Challenges and prospects in ocean circulation models. *Frontiers in Marine Science*, **6**, doi:10.3389/fmars.2019.00065.

Frankignoul, C., A. Czaja, and B. L’Heveder, 1998: Air-sea feedback in the North Atlantic and surface boundary conditions for ocean models. *Journal of Climate*, **11** (9), 2310–2324.

Garrett, C., 2006: Turbulent dispersion in the ocean. *Progress in Oceanography*, **70** (2), 113 – 125, doi:<https://doi.org/10.1016/j.pocean.2005.07.005>, URL <http://www.sciencedirect.com/science/article/pii/S0079661106000577>, gabriel T. Csanady: Understanding the Physics of the Ocean.

Gent, P. R., 2011: The gent–mcwilliams parameterization: 20/20 hindsight. *Ocean Modelling*, **39** (1), 2 – 9, doi:10.1016/j.ocemod.2010.08.002, URL <https://doi.org/10.1016/j.ocemod.2010.08.002>.

Gent, P. R., and J. C. McWilliams, 1990: Isopycnal mixing in ocean circulation models. *Journal of Physical Oceanography*, **20** (1), 150–155, doi:10.1175/1520-0485(1990)020<0150:

IMIOCM)2.0.CO;2, URL [https://doi.org/10.1175/1520-0485\(1990\)020<0150:IMIOCM>2.0.CO;2](https://doi.org/10.1175/1520-0485(1990)020<0150:IMIOCM>2.0.CO;2).

Gent, P. R., J. Willebrand, T. J. McDougall, and J. C. McWilliams, 1995: Parameterizing eddy-induced tracer transports in ocean circulation models. *Journal of Physical Oceanography*, **25** (4), 463–474, doi:10.1175/1520-0485(1995)025<0463:PEITTI>2.0.CO;2, URL [https://doi.org/10.1175/1520-0485\(1995\)025<0463:PEITTI>2.0.CO;2](https://doi.org/10.1175/1520-0485(1995)025<0463:PEITTI>2.0.CO;2).

Gnanadesikan, A., M.-A. Pradal, and R. Abernathey, 2015: Isopycnal mixing by mesoscale eddies significantly impacts oceanic anthropogenic carbon uptake. *Geophysical Research Letters*, **42** (11), 4249–4255, doi:10.1002/2015GL064100, URL <https://agupubs.onlinelibrary.wiley.com/doi/abs/10.1002/2015GL064100>.

Gnanadesikan, A., A. Russell, M.-A. Pradal, and R. Abernathey, 2017: Impact of Lateral Mixing in the Ocean on El Nino in a Suite of Fully Coupled Climate Models. *Journal of Advances in Modeling Earth Systems*, **9** (7), 2493–2513, doi:10.1002/2017MS000917, URL <https://agupubs.onlinelibrary.wiley.com/doi/abs/10.1002/2017MS000917>.

Griffies, S. M., 1998: The gent–mcwilliams skew flux. *Journal of Physical Oceanography*, **28** (5), 831–841, doi:10.1175/1520-0485(1998)028<0831:TGMSF>2.0.CO;2.

Griffies, S. M., 2004: *Fundamentals of Ocean Climate Models*. Princeton University Press, URL <http://www.jstor.org/stable/j.ctv301gzg>.

Groeskamp, S., P. M. Barker, T. J. McDougall, R. P. Abernathey, and S. M. Griffies, 2019: Venm: An algorithm to accurately calculate neutral slopes and gradients. *Journal of Advances in Modeling Earth Systems*, **11** (7), 1917–1939, doi:10.1029/2019MS001613,

URL <https://agupubs.onlinelibrary.wiley.com/doi/abs/10.1029/2019MS001613>, <https://agupubs.onlinelibrary.wiley.com/doi/pdf/10.1029/2019MS001613>.

Hallberg, R., 2013: Using a resolution function to regulate parameterizations of oceanic mesoscale eddy effects. *Ocean Modelling*, **72**, 92 – 103, doi:10.1016/j.ocemod.2013.08.007, URL <https://doi.org/10.1016/j.ocemod.2013.08.007>.

Hausmann, U., and A. Czaja, 2012: The observed signature of mesoscale eddies in sea surface temperature and the associated heat transport. *Deep Sea Research Part I: Oceanographic Research Papers*, **70**, 60 – 72, doi:<https://doi.org/10.1016/j.dsr.2012.08.005>, URL <http://www.sciencedirect.com/science/article/pii/S0967063712001720>.

Herterich, K., and K. Hasselmann, 1987: Extraction of mixed layer advection velocities, diffusion coefficients, feedback factors and atmospheric forcing parameters from the statistical analysis of north pacific sst anomaly fields. *Journal of Physical Oceanography*, **17** (12), 2145–2156, doi:10.1175/1520-0485(1987)017<2145:EOMLAV>2.0.CO;2, URL [https://doi.org/10.1175/1520-0485\(1987\)017<2145:EOMLAV>2.0.CO;2](https://doi.org/10.1175/1520-0485(1987)017<2145:EOMLAV>2.0.CO;2).

Jansen, M. F., A. Adcroft, S. Khani, and H. Kong, 2019: Toward an Energetically Consistent, Resolution Aware Parameterization of Ocean Mesoscale Eddies. *Journal of Advances in Modeling Earth Systems*, **0** (0), doi:10.1029/2019MS001750, URL <https://agupubs.onlinelibrary.wiley.com/doi/abs/10.1029/2019MS001750>.

Jeffress, S., and T. Haine, 2014a: Correlated signals and causal transport in ocean circulation. *Quarterly Journal of the Royal Meteorological Society*, **140** (684), 2375–2382.

Jeffress, S., and T. Haine, 2014b: Estimating sea-surface temperature transport fields from stochastically-forced fluctuations. *New Journal of Physics*, **16** (10), 105001.

- Klocker, A., and R. Abernathey, 2014: Global patterns of mesoscale eddy properties and diffusivities. *Journal of Physical Oceanography*, **44** (3), 1030–1046, doi:10.1175/JPO-D-13-0159.1.
- Klocker, A., R. Ferrari, and J. H. LaCasce, 2012a: Estimating suppression of eddy mixing by mean flows. *Journal of Physical Oceanography*, **42** (9), 1566–1576.
- Klocker, A., R. Ferrari, J. H. Lacasce, and S. T. Merrifield, 2012b: Reconciling float-based and tracer-based estimates of lateral diffusivities. *Journal of Marine Research*, **70** (4), 569–602, doi:doi:10.1357/002224012805262743.
- Klocker, A., and D. P. Marshall, 2014: Advection of baroclinic eddies by depth mean flow. *Geophysical Research Letters*, **41** (10), 3517–3521, doi:10.1002/2014GL060001, URL <http://dx.doi.org/10.1002/2014GL060001>.
- LaCasce, J., 2008: Statistics from lagrangian observations. *Progress in Oceanography*, **77** (1), 1 – 29, doi:<https://doi.org/10.1016/j.pocean.2008.02.002>, URL <http://www.sciencedirect.com/science/article/pii/S0079661108000232>.
- Le Sommer, J., F. d’Ovidio, and G. Madec, 2011: Parameterization of subgrid stirring in eddy resolving ocean models. part 1: Theory and diagnostics. *Ocean Modelling*, **39** (1), 154 – 169, doi:10.1016/j.ocemod.2011.03.007, URL <https://doi.org/10.1016/j.ocemod.2011.03.007>.
- Lumpkin, R., and G. C. Johnson, 2013: Global ocean surface velocities from drifters: Mean, variance, El Nino–Southern Oscillation response, and seasonal cycle. *Journal of Geophysical Research: Oceans*, **118** (6), 2992–3006.

- Mak, J., J. R. Maddison, D. P. Marshall, and D. R. Munday, 2018: Implementation of a geometrically informed and energetically constrained mesoscale eddy parameterization in an ocean circulation model. *Journal of Physical Oceanography*, **0** (**0**), null, doi:10.1175/JPO-D-18-0017.1, URL <https://doi.org/10.1175/JPO-D-18-0017.1>.
- Marshall, J., A. Adcroft, C. Hill, L. Perelman, and C. Heisey, 1997: A finite-volume, incompressible navier stokes model for studies of the ocean on parallel computers. *Journal of Geophysical Research: Oceans*, **102** (**C3**), 5753–5766, doi:10.1029/96JC02775, URL <https://agupubs.onlinelibrary.wiley.com/doi/abs/10.1029/96JC02775>.
- Marshall, J., E. Shuckburgh, H. Jones, and C. Hill, 2006: Estimates and implications of surface eddy diffusivity in the southern ocean derived from tracer transport. *Journal of Physical Oceanography*, **36** (**9**), 1806–1821, doi:10.1175/JPO2949.1, URL <https://doi.org/10.1175/JPO2949.1>.
- Nakamura, N., 1996: Two-Dimensional Mixing, Edge Formation, and Permeability Diagnosed in an Area Coordinate. *Journal of the Atmospheric Sciences*, **53** (**11**), 1524–1537, doi:10.1175/1520-0469(1996)053<1524:TDMEFA>2.0.CO;2, URL [https://doi.org/10.1175/1520-0469\(1996\)053<1524:TDMEFA>2.0.CO;2](https://doi.org/10.1175/1520-0469(1996)053<1524:TDMEFA>2.0.CO;2).
- Newman, M., 2007: Interannual to decadal predictability of tropical and north pacific sea surface temperatures. *Journal of Climate*, **20** (**11**), 2333–2356, doi:10.1175/JCLI4165.1.
- Nummelin, A., S. Jeffress, and T. Haine, 2018: Statistical inversion of surface ocean kinematics from satellite sea surface temperature observations. *J. Atmos. Oceanic Technol.*
- Okubo, A., 1971: Oceanic diffusion diagrams. *Deep Sea Research and Oceanographic Abstracts*, **18** (**8**), 789 – 802, doi:[https://doi.org/10.1016/0011-7471\(71\)90046-5](https://doi.org/10.1016/0011-7471(71)90046-5), URL

<http://www.sciencedirect.com/science/article/pii/0011747171900465>.

Ollitrault, M., C. Gabillet, and A. C. De Verdier, 2005: Open ocean regimes of relative dispersion. *Journal of Fluid Mechanics*, **533**, 381–407, doi:10.1017/S0022112005004556.

Osborn, T. R., and C. S. Cox, 1972: Oceanic fine structure. *Geophysical Fluid Dynamics*, **3** (1), 321–345, doi:10.1080/03091927208236085, URL <https://doi.org/10.1080/03091927208236085>.

Ostrovskii, A., and J. Font, 2003: Advection and dissipation rates in the upper ocean mixed layer heat anomaly budget over the North Atlantic in summer. *Journal of Geophysical Research: Oceans (1978–2012)*, **108** (C12).

Ostrovskii, A. G., and L. I. Piterbarg, 2000: Inversion of upper ocean temperature time series for entrainment, advection, and diffusivity. *Journal of Physical Oceanography*, **30** (1), 201–214.

Pearson, B., B. Fox-Kemper, S. Bachman, and F. Bryan, 2017: Evaluation of scale-aware subgrid mesoscale eddy models in a global eddy-rich model. *Ocean Modelling*, **115**, 42–58, doi:10.1016/j.ocemod.2017.05.007, URL <https://doi.org/10.1016/j.ocemod.2017.05.007>.

Penland, C., and L. M. Hartten, 2014: Stochastic forcing of north tropical Atlantic sea surface temperatures by the North Atlantic Oscillation. *Geophysical Research Letters*, **41** (6), 2126–2132, doi:10.1002/2014GL059252, 2014GL059252.

Penland, C., and T. Magorian, 1993: Prediction of Niño 3 Sea Surface Temperatures Using Linear Inverse Modeling. *Journal of Climate*, **6** (6), 1067–1076, doi:10.1175/1520-0442(1993)006<1067:PONSST>2.0.CO;2.

- Penland, C., and L. Matrosova, 1998: Prediction of Tropical Atlantic Sea Surface Temperatures Using Linear Inverse Modeling. *Journal of Climate*, **11** (3), 483–496, doi:10.1175/1520-0442(1998)011<0483:POTASS>2.0.CO;2.
- Penland, C., and P. D. Sardeshmukh, 1995: The Optimal Growth of Tropical Sea Surface Temperature Anomalies. *Journal of Climate*, **8** (8), 1999–2024, doi:10.1175/1520-0442(1995)008<1999:TOGOTS>2.0.CO;2.
- Piterbarg, L., and A. Ostrovskii, 1997: *Advection and diffusion in random media: implications for sea surface temperature anomalies*. Springer.
- Poje, A. C., A. C. Haza, T. M. Özgökmen, M. G. Magaldi, and Z. D. Garraffo, 2010: Resolution dependent relative dispersion statistics in a hierarchy of ocean models. *Ocean Modelling*, **31** (1), 36 – 50, doi:<https://doi.org/10.1016/j.ocemod.2009.09.002>, URL <http://www.sciencedirect.com/science/article/pii/S1463500309001826>.
- Prandtl, L., 1925: 7. Bericht über Untersuchungen zur ausgebildeten Turbulenz. *Zeitschrift Angewandte Mathematik und Mechanik*, **5** (2), 136–139, doi:10.1002/zamm.19250050212.
- Ramshaw, J. D., 1985: Conservative rezoning algorithm for generalized two-dimensional meshes. *Journal of Computational Physics*, **59** (2), 193 – 199, doi:[https://doi.org/10.1016/0021-9991\(85\)90141-X](https://doi.org/10.1016/0021-9991(85)90141-X).
- Redi, M. H., 1982: Oceanic isopycnal mixing by coordinate rotation. *Journal of Physical Oceanography*, **12** (10), 1154–1158, doi:10.1175/1520-0485(1982)012<1154:OIMBCR>2.0.CO;2, URL [https://doi.org/10.1175/1520-0485\(1982\)012<1154:OIMBCR>2.0.CO;2](https://doi.org/10.1175/1520-0485(1982)012<1154:OIMBCR>2.0.CO;2).

- Reynolds, R. W., T. M. Smith, C. Liu, D. B. Chelton, K. S. Casey, and M. G. Schlax, 2007: Daily high-resolution-blended analyses for sea surface temperature. *Journal of Climate*, **20** (22), 5473–5496.
- Rhines, P. B., and W. R. Young, 1983: How rapidly is a passive scalar mixed within closed streamlines? *Journal of Fluid Mechanics*, **133**, 133–145, doi:10.1017/S0022112083001822.
- Rio, M.-H., S. Mulet, and N. Picot, 2014: Beyond goce for the ocean circulation estimate: Synergetic use of altimetry, gravimetry, and in situ data provides new insight into geostrophic and ekman currents. *Geophysical Research Letters*, **41** (24), 8918–8925, doi:10.1002/2014GL061773, URL <https://agupubs.onlinelibrary.wiley.com/doi/abs/10.1002/2014GL061773>.
- Rio, M.-H., R. Santoleri, R. Bourdalle-Badie, A. Griffa, L. Piterbarg, and G. Taburet, 2016: Improving the altimeter-derived surface currents using high-resolution sea surface temperature data: A feasibility study based on model outputs. *Journal of Atmospheric and Oceanic Technology*, **33** (12), 2769–2784, doi:10.1175/JTECH-D-16-0017.1, URL <https://doi.org/10.1175/JTECH-D-16-0017.1>.
- Roach, C. J., D. Balwada, and K. Speer, 2018: Global observations of horizontal mixing from argo float and surface drifter trajectories. *Journal of Geophysical Research: Oceans*, **123** (7), 4560–4575, doi:10.1029/2018JC013750, URL <https://agupubs.onlinelibrary.wiley.com/doi/abs/10.1029/2018JC013750>.
- Sen, P. K., 1968: Estimates of the regression coefficient based on kendall’s tau. *Journal of the American Statistical Association*, **63** (324), 1379–1389, URL <http://www.jstor.org/stable/2285891>.

- Shuckburgh, E., H. Jones, J. Marshall, and C. Hill, 2009: Robustness of an Effective Diffusivity Diagnostic in Oceanic Flows. *Journal of Physical Oceanography*, **39** (9), 1993–2009, doi:10.1175/2009JPO4122.1, URL <https://doi.org/10.1175/2009JPO4122.1>.
- Smith, K. S., and J. Marshall, 2009: Evidence for Enhanced Eddy Mixing at Middepth in the Southern Ocean. *Journal of Physical Oceanography*, **39** (1), 50–69, doi:10.1175/2008JPO3880.1, URL <https://doi.org/10.1175/2008JPO3880.1>.
- Taylor, G., 1953: Dispersion of soluble matter in solvent flowing slowly through a tube. *Proceedings of the Royal Society of London A: Mathematical, Physical and Engineering Sciences*, **219** (1137), 186–203, doi:10.1098/rspa.1953.0139, URL <http://rspa.royalsocietypublishing.org/content/219/1137/186>.
- Theil, H., 1950: A rank-invariant method of linear and polynomial regression analysis i, ii, and iii. *Nederl. Akad. Wetensch., Proc.*, **53**, 386–392, 521–525, 1397–1412, URL <http://www.jstor.org/stable/2285891>.
- Vallis, G. K., 2006: *Atmospheric and Oceanic Fluid Dynamics*. Cambridge University Press, Cambridge, U.K., 745 pp.
- van Sebille, E., S. Waterman, A. Barthel, R. Lumpkin, S. R. Keating, C. Fogwill, and C. Turney, 2015: Pairwise surface drifter separation in the western pacific sector of the southern ocean. *Journal of Geophysical Research: Oceans*, **120** (10), 6769–6781, doi:10.1002/2015JC010972, URL <https://agupubs.onlinelibrary.wiley.com/doi/abs/10.1002/2015JC010972>.
- Villas Boas, A. B., O. T. Sato, A. Chaigneau, and G. P. Castelao, 2015: The signature of mesoscale eddies on the air-sea turbulent heat fluxes in the south atlantic

ocean. *Geophysical Research Letters*, **42** (6), 1856–1862, doi:10.1002/2015GL063105, URL <https://agupubs.onlinelibrary.wiley.com/doi/abs/10.1002/2015GL063105>.

Vollmer, L., and C. Eden, 2013: A global map of meso-scale eddy diffusivities based on linear stability analysis. *Ocean Modelling*, **72**, 198 – 209, doi:<https://doi.org/10.1016/j.ocemod.2013.09.006>.

Wagner, P., S. Rühls, F. U. Schwarzkopf, I. M. Koszalka, and A. Biastoch, 2019: Can Lagrangian Tracking Simulate Tracer Spreading in a High-Resolution Ocean General Circulation Model? *Journal of Physical Oceanography*, **49** (5), 1141–1157, doi:10.1175/JPO-D-18-0152.1.

Weizsäcker, C. F. v., 1948: Das spektrum der turbulenz bei großen reynoldsschen zahlen. *Zeitschrift für Physik*, **124** (7), 614–627, doi:10.1007/BF01668898, URL <https://doi.org/10.1007/BF01668898>.

Young, W. R., P. B. Rhines, and C. J. R. Garrett, 1982: Shear-Flow Dispersion, Internal Waves and Horizontal Mixing in the Ocean. *Journal of Physical Oceanography*, **12** (6), 515–527, doi:10.1175/1520-0485(1982)012<0515:SFDIWA>2.0.CO;2.

Zanna, L., 2012: Forecast skill and predictability of observed Atlantic sea surface temperatures. *Journal of Climate*, **25** (14), 5047–5056.

Zanna, L., 2019: Ocean Transport and Eddy Energy; Proposal to CVP - Climate Process Teams - Translating Ocean and/or Atmospheric Process Understanding to Improve Climate Models;. doi:10.6084/m9.figshare.10105922.v1, URL <https://figshare.com/articles/journal.contribution/Proposal/10105922>.

- Zanna, L., P. P. Mana, J. Anstey, T. David, and T. Bolton, 2017: Scale-aware deterministic and stochastic parametrizations of eddy-mean flow interaction. *Ocean Modelling*, **111**, 66 – 80, doi:<https://doi.org/10.1016/j.ocemod.2017.01.004>.
- Zhuang, J., R. Dussin, A. Jüling, and S. Rasp, 2020: JiaweiZhuang/xESMF: v0.3.0 Adding ESMF.LocStream capabilities. Zenodo, URL <https://doi.org/10.5281/zenodo.3700105>, doi:10.5281/zenodo.3700105.
- Zhurbas, V., D. Lyzhkov, and N. Kuzmina, 2014: Drifter-derived estimates of lateral eddy diffusivity in the world ocean with emphasis on the indian ocean and problems of parameterisation. *Deep Sea Research Part I: Oceanographic Research Papers*, **83**, 1 – 11, doi:<https://doi.org/10.1016/j.dsr.2013.09.001>, URL <http://www.sciencedirect.com/science/article/pii/S0967063713001854>.

LIST OF TABLES

Table 1. List of selected symbols and their definitions	49
Table 2. The slope exponent n in the $\kappa \propto l^n$ scaling for l between 40 km and 200 km. The selected ocean regions are the same as in Figure 3. We estimate n using the Theil-Sen regression estimate (Theil 1950; Sen 1968) in log-log space for each of the 60 ensemble members (i.e. we combine the diffusivity estimates that are based on both 10-year long and 5-year long overlapping data-segments). We then have a 60 member distribution of the slope exponent n from which we show the 5%, 50%, and 95% percentiles.	50

TABLE 1. List of selected symbols and their definitions

Symbol	definition
\mathbf{K}_t	Diffusion tensor.
\mathbf{K}_a	The antisymmetric part of \mathbf{K}_t .
\mathbf{K}	The symmetric part of \mathbf{K}_t .
κ	Magnitude of \mathbf{K} .
κ_{SSTA}	Magnitude of the sea surface temperature based diffusion estimate.
κ_{MITgem}	Magnitude of the idealized tracer based diffusion estimate.
κ_s	Magnitude of the theoretical small scale diffusivity estimate (based on mixing length theory).
κ_{l1}	Magnitude of the theoretical estimate of sub-grid scale diffusion due to large scale stirring following Le Sommer et al. (2011).
κ_{l2}	Integral formulation of κ_{l1} designed to capture shear at scales much larger than the local grid size.
u_{rms}	Root mean square velocity.
l	Generic symbol for a length scale.
l_{eddy}	Eddy length scale.
h	Filter size.
h_0	The smallest filter size (Gaussian filter with standard deviation of 3 grid cells).
$\Delta x, \Delta y$	Grid size of the data-product which the MicroInverse method uses.
$\Delta x_{MI}, \Delta y_{MI}$	The effective length scale of the MicroInverse diffusivity estimates ($2 \times \Delta x, 2 \times \Delta y$).
x, χ	symbol for a tracer field (a vector and a matrix).
$\mathbf{B}, \hat{\mathbf{B}}$	Transport operator and its estimate.

TABLE 2. The slope exponent n in the $\kappa \propto l^n$ scaling for l between 40 km and 200 km. The selected ocean regions are the same as in Figure 3. We estimate n using the Theil-Sen regression estimate (Theil 1950; Sen 1968) in log-log space for each of the 60 ensemble members (i.e. we combine the diffusivity estimates that are based on both 10-year long and 5-year long overlapping data-segments). We then have a 60 member distribution of the slope exponent n from which we show the 5%, 50%, and 95% percentiles.

Region	Source	n _{5%}	n _{50%}	n _{95%}
TROPICAL PACIFIC	κ_{SSTA}	1.31	1.48	1.51
	κ_{MITgcm}	1.16	1.18	1.20
TROPICAL INDIAN OCEAN	κ_{SSTA}	1.22	1.34	1.44
	κ_{MITgcm}	1.03	1.06	1.10
TROPICAL ATLANTIC	κ_{SSTA}	1.30	1.48	1.54
	κ_{MITgcm}	1.02	1.04	1.08
NORTH PACIFIC	κ_{SSTA}	0.49	0.60	0.74
	κ_{MITgcm}	0.57	0.63	0.73
NORTH ATLANTIC	κ_{SSTA}	0.76	0.93	1.11
	κ_{MITgcm}	0.99	1.05	1.13
SOUTH INDIAN OCEAN	κ_{SSTA}	0.56	0.61	0.68
	κ_{MITgcm}	0.88	0.92	0.96
SOUTH ATLANTIC	κ_{SSTA}	0.65	0.72	0.83
	κ_{MITgcm}	0.79	0.86	0.95

LIST OF FIGURES

- Fig. 1.** Illustration of the grid used in the inversion and the related length scales. If a data product has a resolution of Δx (or Δy in y direction), the resulting MicroInverse estimate will have an effective resolution of Δx_{MI} (Δy_{MI}) because the inversion is based on discretization at grid resolution. 53
- Fig. 2.** Spatial distribution (a-b) and zonal distribution (d) of κ from MicroInverse at 0.5° resolution using sea surface temperature anomalies (SSTA; a) and the idealized MITgcm simulations (b). Red contours in panels a–b show where kinetic energy is $0.25\text{m}^2\text{s}^{-2}$. The white shading in each panel indicates regions where the estimates are not robust as the signal-to-noise ratio (ensemble median/ensemble standard deviation) is less than 2. Note that all the fields are smoothed with a 0.5° wide Gaussian filter. In panel d, the solid line shows the ensemble median zonal median, the darker narrow shading shows the 5%–95% ensemble spread of the zonal median, and the shading shows the 25%–75% range in the zonal band of the ensemble median. 54
- Fig. 3.** Scale dependence of diffusivity on length scale (l) for (a) sea surface temperature and (b) idealized tracer based diffusivity in selected ocean regions (d). The vertical bars in panels a and b indicate the ensemble spread as follows: solid (dashed) lines use the ensemble with 10-year (5-year) segments, and thick (thin) lines indicate 25%–75% (5%–95%) percentile range. The black lines in the background (panels a–c) show the slopes $l^{2/3}$ (dashed), l (dotted), and $l^{4/3}$ (solid) for guidance. 55
- Fig. 4.** Spatial distribution (a-b) and zonal distribution (c) of the slope exponent n in the $\kappa \propto l^n$ scaling for l between 40 km and 200 km. Similar to Fig. 2, we show slopes based on temperature anomalies (SSTA; a) and the idealized MITgcm simulations (b). The white shading indicates where the estimates are not robust (the ensemble median/ensemble standard deviation is less than 3). The black contours show the mean eddy size binned to 0.25° grid from the eddy-trajectory atlas (version DT 2.0exp; <https://www.avisio.altimetry.fr/en/data/products/value-added-products/global-mesoscale-eddy-trajectory-product.html>). In panel d, the solid line shows the ensemble median zonal median, the darker narrow shading shows the 5%–95% ensemble spread of the zonal median and the lighter shading shows the 25%–75% range in the zonal band. The gray dashed vertical lines show the $2/3$, 1 , and $4/3$ slopes as in Figure 3. 56
- Fig. 5.** Spatial distribution (a–c) and zonal distribution (d) of the magnitude of the theoretical diffusivity estimates at 0.5° resolution, similar to Fig 2: (a) sub-gridscale stirring κ_s from (C2), (b) shear κ_{l1} from (C3), and (c) large scale shear κ_{l2} from (C4). Red contours in panels a–c show where kinetic energy is $0.25\text{m}^2\text{s}^{-2}$. Here we have scaled κ_s , κ_{l1} , and κ_{l2} according to global linear fit to κ_{SSTA} (see Fig. 6) with the regression slopes: 0.16, 0.08, and 0.04; and biases: $206\text{ m}^2\text{ s}^{-1}$, $117\text{ m}^2\text{ s}^{-1}$, $60\text{ m}^2\text{ s}^{-1}$; respectively. . In panel d, solid lines show the zonal median (same scaling as above), while the shaded areas show the 25%–75% range in the zonal band. 57
- Fig. 6.** Scatter plot and spatial correlation between MicroInverse diffusivity estimates (Fig. 2) and linear least squares fit of the theoretical diffusivity estimates (Fig. 5). Color of the dots indicates the absolute value of the latitude. In addition we show 4 squared (Pearson) correlation coefficients at diferent latitude bands

(shown in the subscript). The dashed gray line in the background shows the 1-to-1 relationship. 58

Fig. 7. Same as Fig 3, but for the theoretical diffusivity estimates: (a) sub-gridscale stirring κ_s from (C2), (b) shear κ_{l1} from (C3), and (c) large scale shear κ_{l2} from (C4). Here we have applied the same linear scaling as in Fig. 5. 59

Fig. 8. Same as Fig 4 (scales between 40 km and 200 km), except for the theoretical diffusivity estimates: (a) sub-gridscale stirring κ_s from (C2), (b) shear κ_l from (C3), and (c) large scale shear κ_{l2} from (C4). The white shading indicates regions where the slope is negative. In panel d, the solid lines show the zonal median and the shaded areas show the 25%–75% range in the zonal band. The gray dashed vertical lines show the 2/3, 1, and 4/3 slopes as in Figures 3 and 7. 60

Fig. 9. Error characteristics of the combined theory compared to the ensemble mean κ_{MITgcm} in the tropics (equatorward of 15° in both hemispheres), and in the midlatitudes ($15\text{--}60^\circ$ in both hemispheres). The upper rows (a–d) show the combination of (C2) and (C3) and the lower row (e–h) shows the combination of (C2) and (C4). The color shows the mean absolute percentage error (MAPE), white contours show squared Pearson correlation coefficient, black contours show linear least-squares regression slope, and red contours show the area averaged contribution of large scale shear versus sub-gridscale stirring in percentage (0–100%). Based on these comparison metrics, the thick red ellipses suggest an optimal (b_1, b_2) space (small MAPE, high correlation, regression slope ~ 1). 61

Fig. 10. Schematic illustration of the large scale shear and sub-gridscale stirring driven mixing. Large scale shear driven mixing is a self similar in respect to the length scale whereas sub-gridscale stirring becomes (relatively) less effective as the grid scale is much above the length scale of the dominating eddy scale. 62

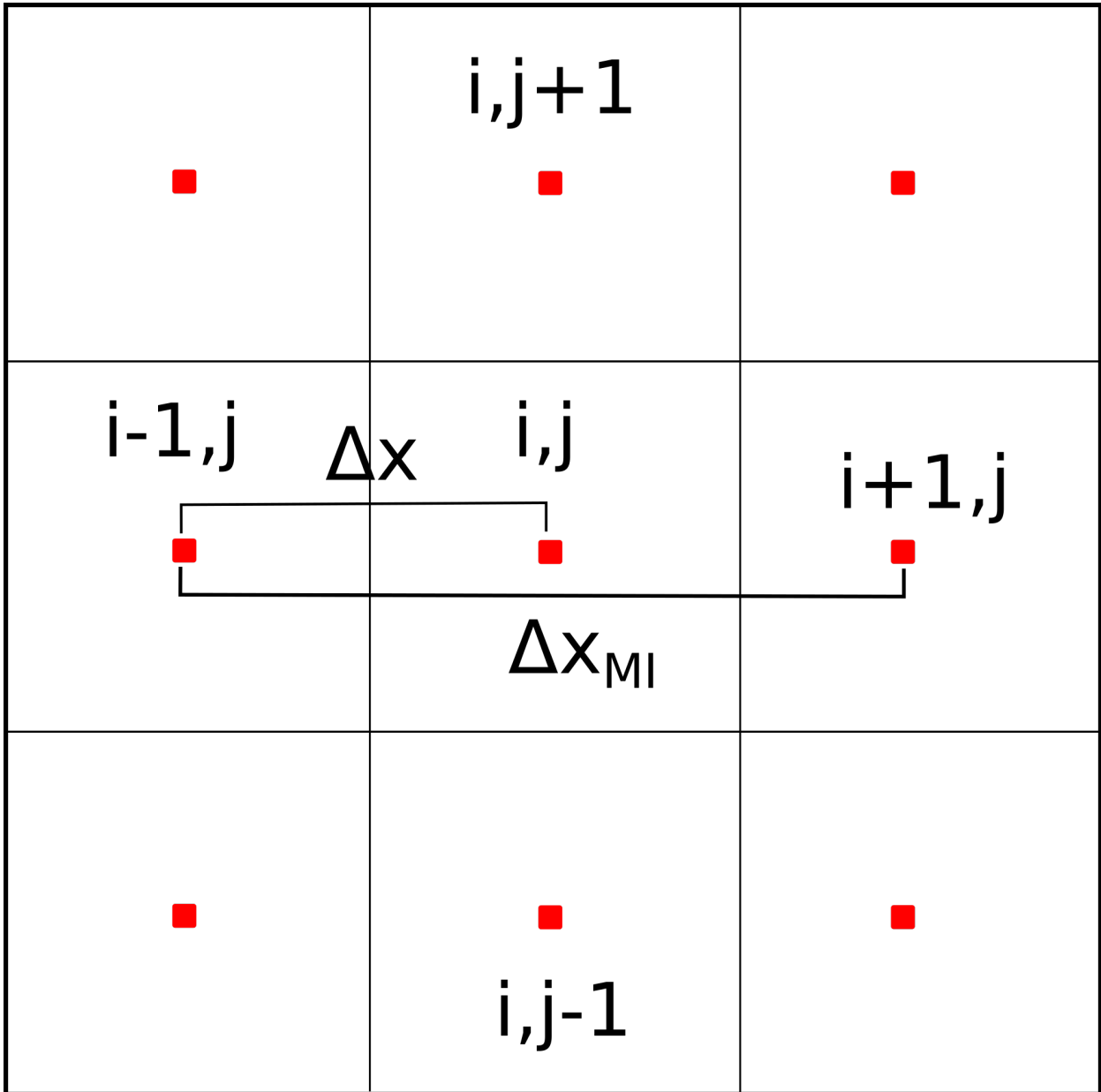


FIG. 1. Illustration of the grid used in the inversion and the related length scales. If a data product has a resolution of Δx (or Δy in y direction), the resulting MicroInverse estimate will have an effective resolution of Δx_{MI} (Δy_{MI}) because the inversion is based on discretization at grid resolution.

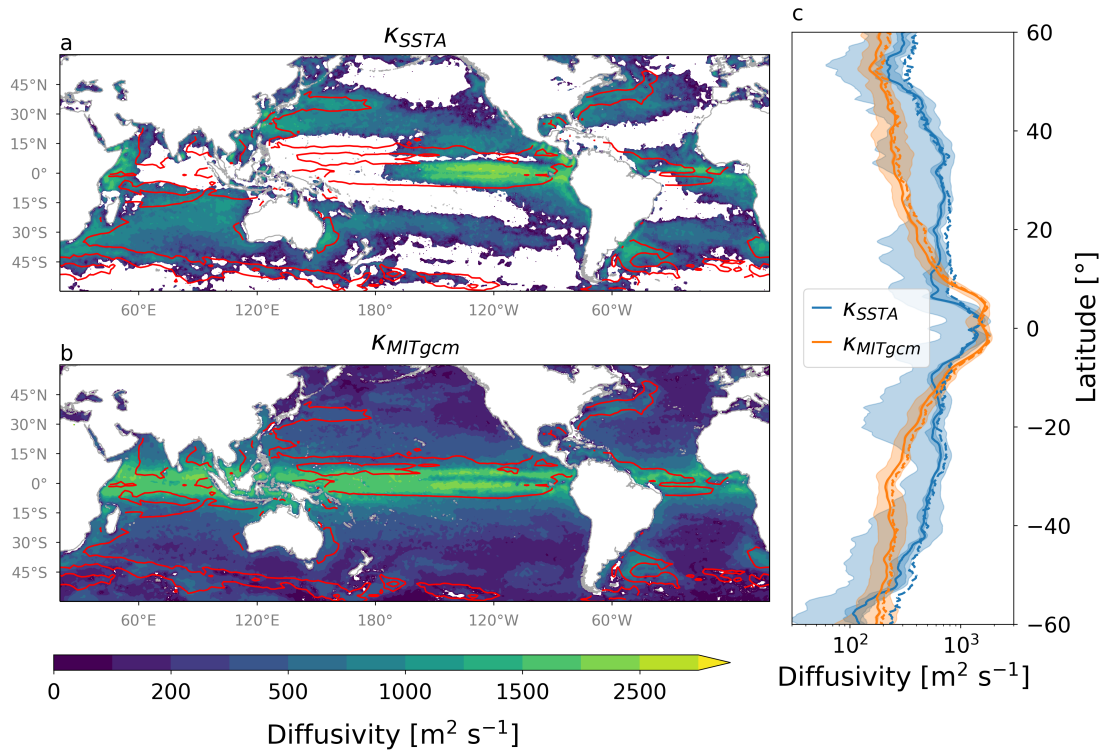


FIG. 2. Spatial distribution (a-b) and zonal distribution (d) of κ from MicroInverse at 0.5° resolution using sea surface temperature anomalies (SSTA; a) and the idealized MITgcm simulations (b). Red contours in panels a–b show where kinetic energy is $0.25 m^2 s^{-2}$. The white shading in each panel indicates regions where the estimates are not robust as the signal-to-noise ratio (ensemble median/ensemble standard deviation) is less than 2. Note that all the fields are smoothed with a 0.5° wide Gaussian filter. In panel d, the solid line shows the ensemble median zonal median, the darker narrow shading shows the 5%–95% ensemble spread of the zonal median, and the shading shows the 25%–75% range in the zonal band of the ensemble median.

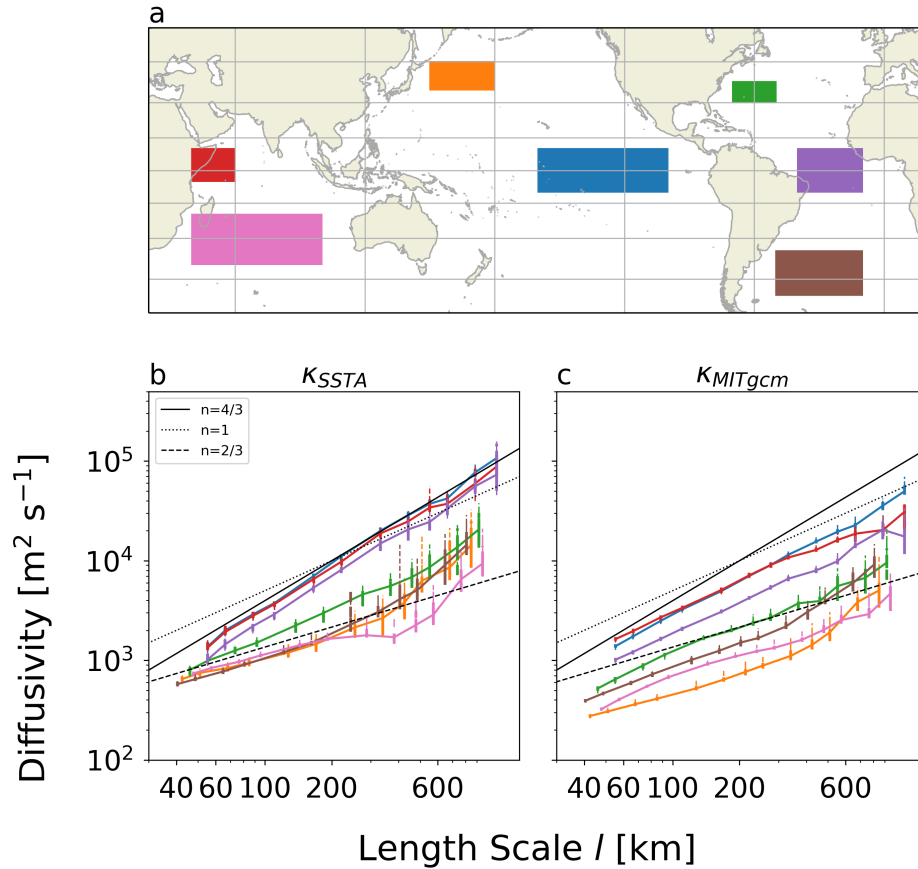


FIG. 3. Scale dependence of diffusivity on length scale (l) for (a) sea surface temperature and (b) idealized tracer based diffusivity in selected ocean regions (d). The vertical bars in panels a and b indicate the ensemble spread as follows: solid (dashed) lines use the ensemble with 10-year (5-year) segments, and thick (thin) lines indicate 25%–75% (5%–95%) percentile range. The black lines in the background (panels a–c) show the slopes $l^{2/3}$ (dashed), l (dotted), and $l^{4/3}$ (solid) for guidance.

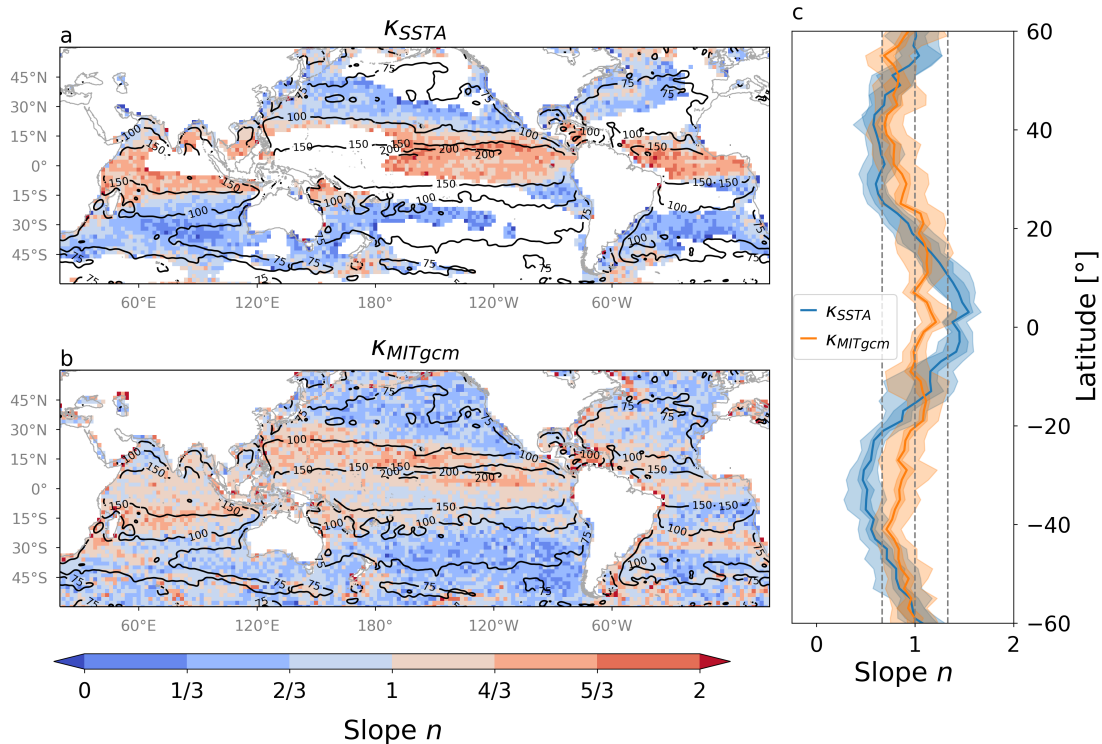


FIG. 4. Spatial distribution (a-b) and zonal distribution (c) of the slope exponent n in the $\kappa \propto l^n$ scaling for l between 40 km and 200 km. Similar to Fig. 2, we show slopes based on temperature anomalies (SSTA; a) and the idealized MITgcm simulations (b). The white shading indicates where the estimates are not robust (the ensemble median/ensemble standard deviation is less than 3). The black contours show the mean eddy size binned to 0.25° grid from the eddy-trajectory atlas (version DT 2.0exp; <https://www.aviso.altimetry.fr/en/data/products/value-added-products/global-mesoscale-eddy-trajectory-product.html>). In panel d, the solid line shows the ensemble median zonal median, the darker narrow shading shows the 5%–95% ensemble spread of the zonal median and the lighter shading shows the 25%–75% range in the zonal band. The gray dashed vertical lines show the 2/3, 1, and 4/3 slopes as in Figure 3.

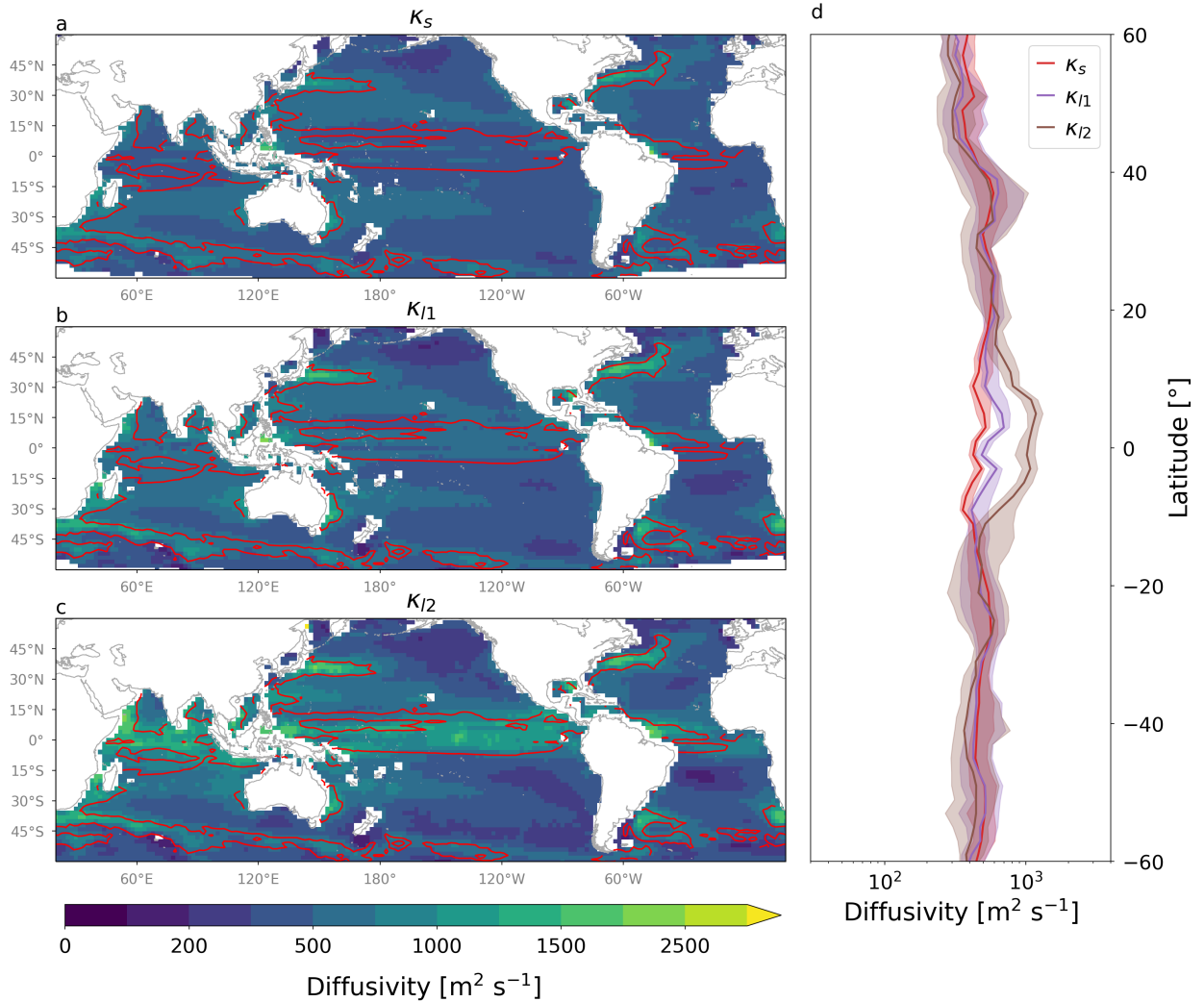


FIG. 5. Spatial distribution (a–c) and zonal distribution (d) of the magnitude of the theoretical diffusivity estimates at 0.5° resolution, similar to Fig 2: (a) sub-gridscale stirring κ_s from (C2), (b) shear κ_{l1} from (C3), and (c) large scale shear κ_{l2} from (C4). Red contours in panels a–c show where kinetic energy is $0.25 \text{m}^2 \text{s}^{-2}$. Here we have scaled κ_s , κ_{l1} , and κ_{l2} according to global linear fit to κ_{SSTA} (see Fig. 6) with the regression slopes: 0.16, 0.08, and 0.04; and biases: $206 \text{m}^2 \text{s}^{-1}$, $117 \text{m}^2 \text{s}^{-1}$, $60 \text{m}^2 \text{s}^{-1}$; respectively. In panel d, solid lines show the zonal median (same scaling as above), while the shaded areas show the 25%–75% range in the zonal band.

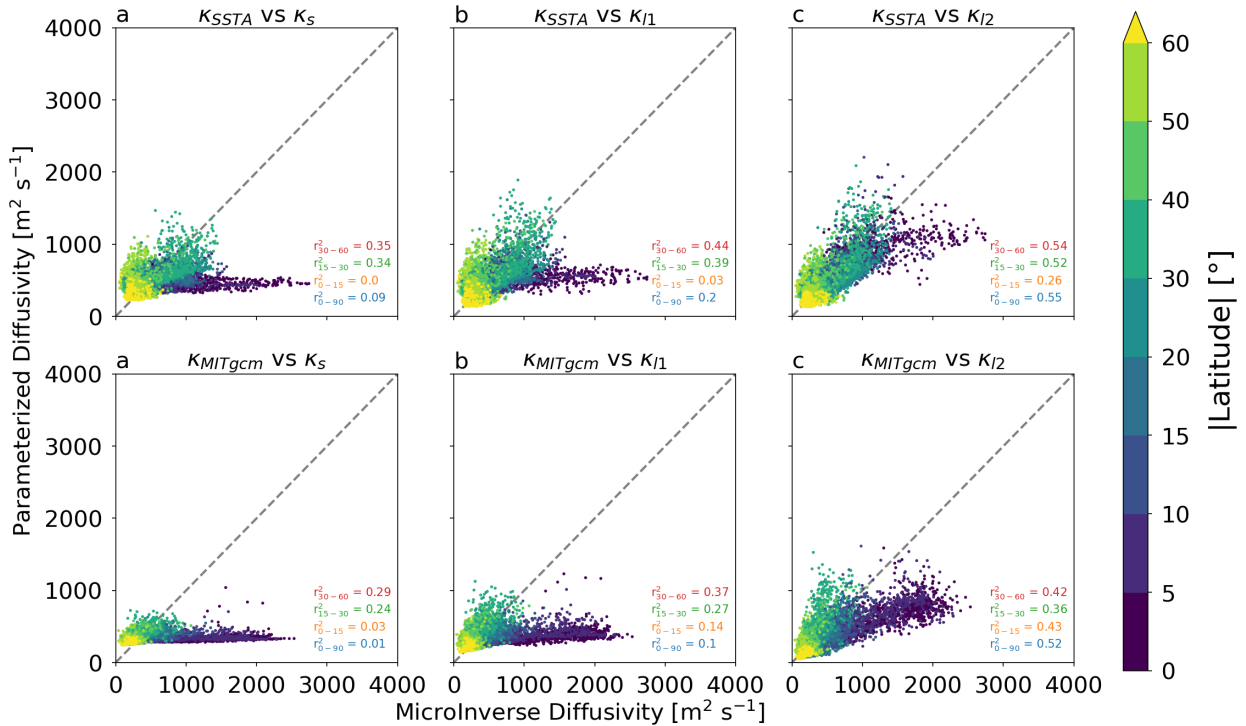


FIG. 6. Scatter plot and spatial correlation between MicroInverse diffusivity estimates (Fig. 2) and linear least squares fit of the theoretical diffusivity estimates (Fig. 5). Color of the dots indicates the absolute value of the latitude. In addition we show 4 squared (Pearson) correlation coefficients at different latitude bands (shown in the subscript). The dashed gray line in the background shows the 1-to-1 relationship.

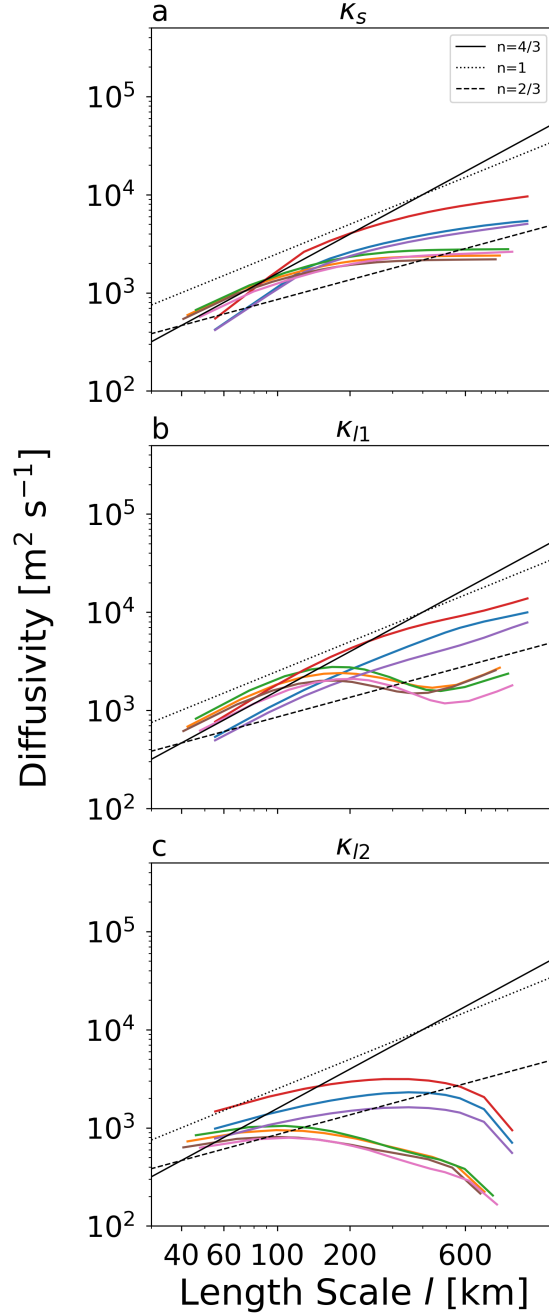


FIG. 7. Same as Fig 3, but for the theoretical diffusivity estimates: (a) sub-grid scale stirring κ_s from (C2), (b) shear κ_{I1} from (C3), and (c) large scale shear κ_{I2} from (C4). Here we have applied the same linear scaling as in Fig. 5.

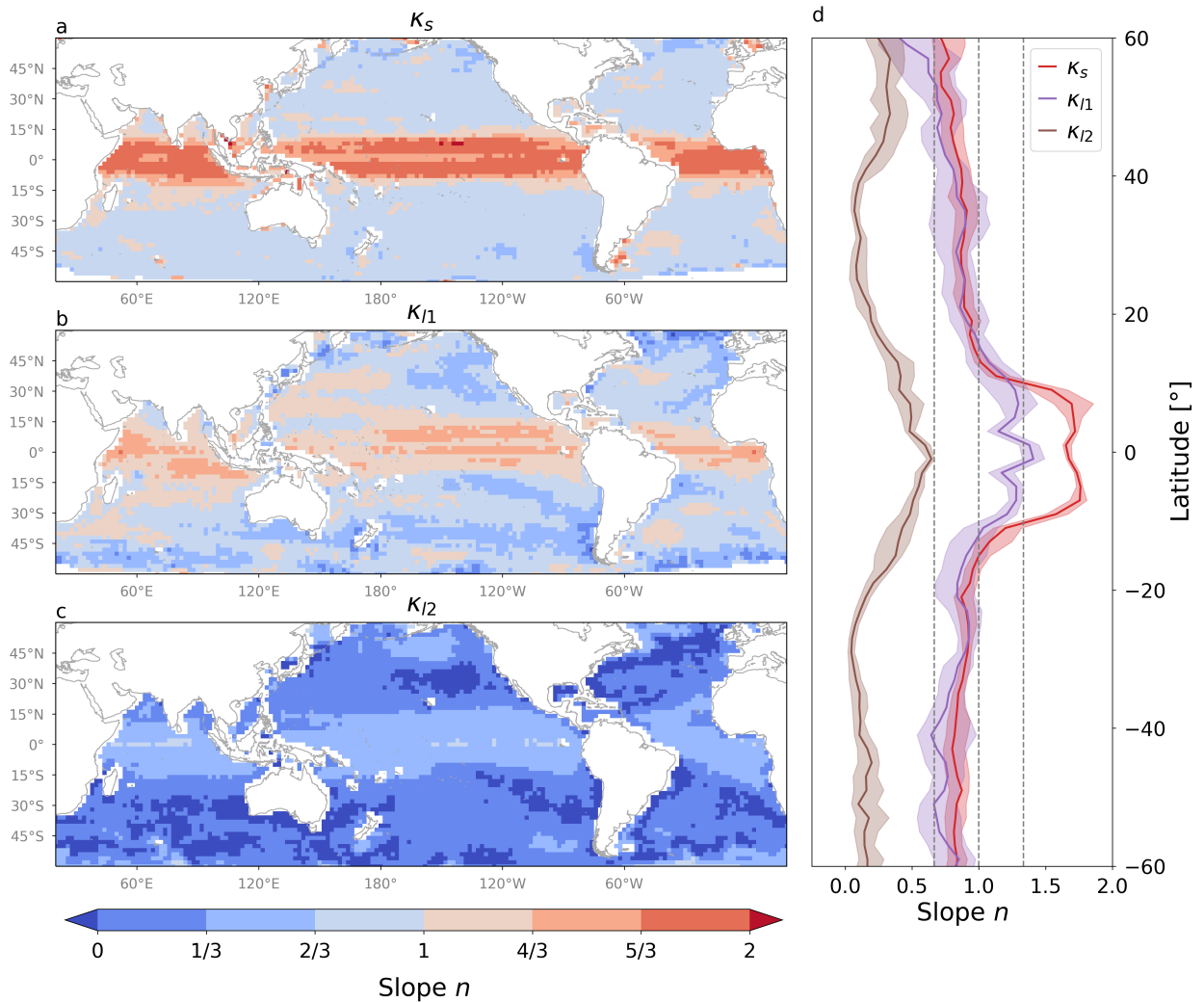


FIG. 8. Same as Fig 4 (scales between 40 km and 200 km), except for the theoretical diffusivity estimates: (a) sub-grid scale stirring κ_s from (C2), (b) shear κ_l from (C3), and (c) large scale shear κ_{l2} from (C4). The white shading indicates regions where the slope is negative. In panel d, the solid lines show the zonal median and the shaded areas show the 25%–75% range in the zonal band. The gray dashed vertical lines show the 2/3, 1, and 4/3 slopes as in Figures 3 and 7.

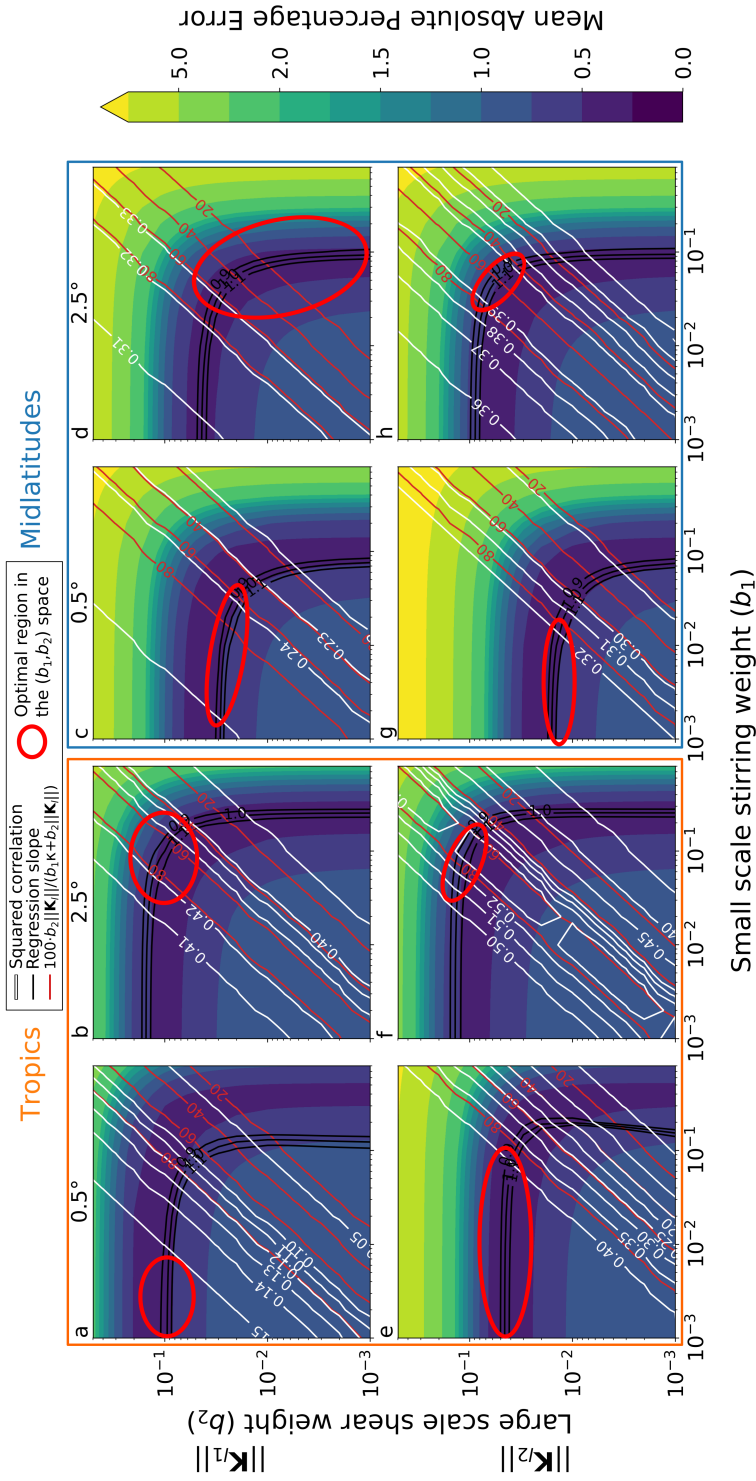


FIG. 9. Error characteristics of the combined theory compared to the ensemble mean $\kappa_{MIT-gcm}$ in the tropics (equatorward of 15° in both hemispheres), and in the midlatitudes ($15-60^\circ$ in both hemispheres). The upper rows (a-d) show the mean absolute percentage error and (C3) and the lower row (e-h) shows the combination of (C2) and (C4). The color shows the mean absolute percentage error (MAPE), white contours show squared Pearson correlation coefficient, black contours show linear least-squares regression slope, and red contours show the area averaged contribution of large scale shear versus sub-gridscale stirring in percentage (0–100%). Based on these comparison metrics, the thick red ellipses suggest an optimal (b_1, b_2) space (small MAPE, high correlation, regression slope ~ 1).

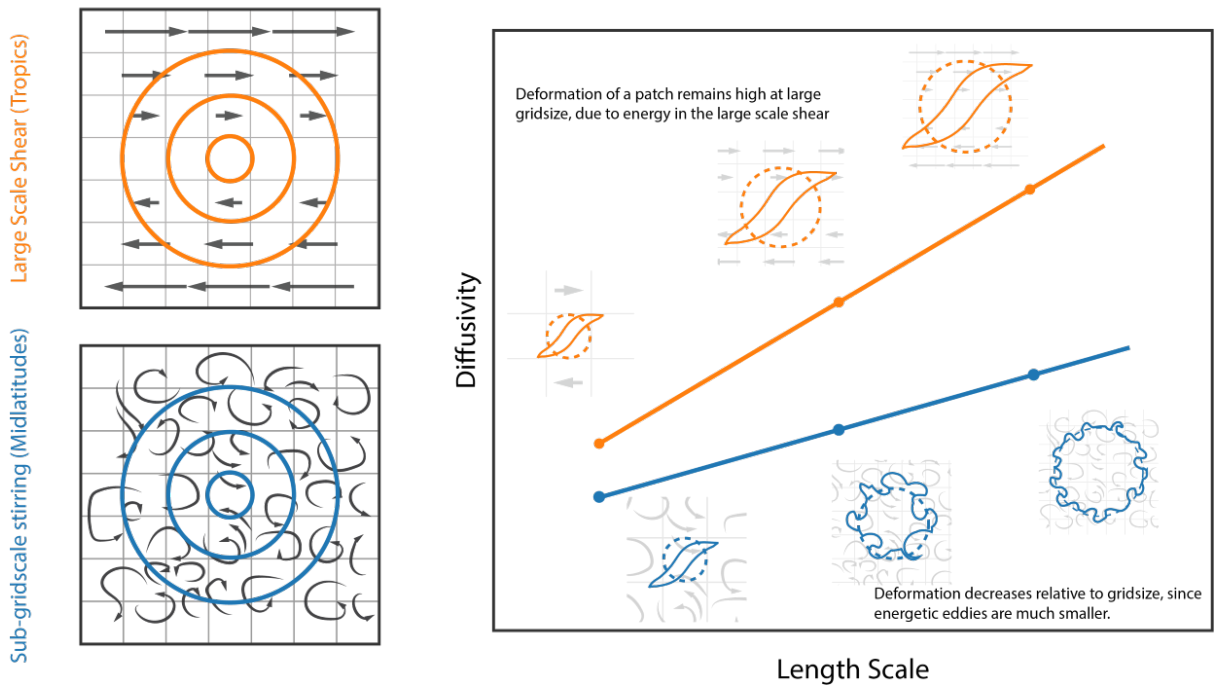


FIG. 10. Schematic illustration of the large scale shear and sub-gridscale stirring driven mixing. Large scale shear driven mixing is self-similar in respect to the length scale whereas sub-gridscale stirring becomes (relatively) less effective as the grid scale is much above the length scale of the dominating eddy scale.